VISCOUS-FLOW ANALYSIS OF A SUBSONIC TRANSPORT AIRCRAFT HIGH-LIFT SYSTEM AND CORRELATION WITH FLIGHT DATA

by

R. C. Potter and C. P. van Dam
Department of Mechanical and Aeronautical Engineering
University of California
Davis, CA 95616

Final Report
Cooperative Agreement NCC1-163

July 1995

Abstract

High-lift system aerodynamics has been gaining attention in recent years. In an effort to improve aircraft performance, comprehensive studies of multi-element airfoil systems are being undertaken in wind-tunnel and flight experiments. Recent developments in Computational Fluid Dynamics (CFD) offer a relatively inexpensive alternative for studying complex viscous flows by numerically solving the Navier-Stokes (N-S) equations. Current limitations in computer resources restrict practical high-lift N-S computations to two dimensions, but CFD predictions can yield tremendous insight into flow structure, interactions between airfoil elements, and effects of changes in airfoil geometry or free-stream conditions. These codes are very accurate when compared to strictly 2-D data provided by wind-tunnel testing, as will be shown here. Yet, additional challenges must be faced in the analysis of a production aircraft wing section, such as that of the NASA Langley Transport Systems Research Vehicle (TSRV). A primary issue is the sweep theory used to correlate 2-D predictions with 3-D flight results, accounting for sweep, taper, and finite wing effects. Other computational issues addressed here include the effects of surface roughness of the geometry, cove shape modeling, grid topology, and transition specification. The sensitivity of the flow to changing free-stream conditions is investigated. In addition, the effects of Gurney flaps on the aerodynamic characteristics of the airfoil system are predicted.

Acknowledgments

This work has been supported by the NASA Langley Research Center through Cooperative Agreement NCC1-163, under the direction of Mr. Long Yip. The author wishes to thank the members of the Flight Research Branch for contributing to a pleasant enviroment in which to develop this study. Special thanks to Professor Cornelis P. van Dam for his inspiration and support, and to Professor Jean Jacques Chattot and Dr. Dimitri J. Mavriplis for their additional review and suggestions in the preparation of this thesis. The author would also like to acknowledge Dr. W. Kyle Anderson, Dr. Shahyar Pirzadeh, and Mr. Steve M. Klausmeyer, for their assistance in the implementation of the computational tools. Finally, thanks to the terrific family and friends who have kept the author smiling.

Table of Contents

List Of Figures

1. Introduction

The performance of modern transport aircraft, in terms of payload and range, is governed by the performance of the high-lift system. The increased lift coefficients required during low speed flight, associated with take-off and landing approach, are achieved by deploying leading-edge slats and trailing-edge slotted flap systems. Design objectives include improved lift and drag characteristics for a given weight and complexity, or decreased weight and complexity for a given C_L requirement. The combination of airfoil elements in a multi-element system can produce remarkably better performance than the sum of individual contributions, and this synergistic interaction involves complex flow physics, making analysis and design difficult. The lack of understanding in this area has inspired numerous comprehensive testing programs, both in wind tunnels and in actual flight[1,2]. Unfortunately, the expense and time involved in instrumentation and data collection severely limits the range of test results. Furthermore, wind tunnel testing can rarely be accomplished at full-scale Reynolds numbers and the extrapolation to flight is non-linear due to various Reynolds number effects[3] (Fig. 1.1).

A potential solution to the challenges of testing programs emerged with the computer revolution of the 1980's and the development of Computational Fluid Dynamics (CFD) methods. Computer simulations of flows were cheaper and much faster than experimental programs, so more configurations could be analyzed, and full-scale flow parameters could be applied. The rapid growth of CFD methods and computer power lead to speculation that CFD would soon render the wind tunnel obsolete. However, all computational methods suffer from limitations in terms of simplifications or assumptions made in the

mathematical model, or hardware limits in CPU power, speed, and memory. Early CFD tools used potential flow and panel methods which solved for inviscid, irrotational flows. Later, Euler methods were applied, allowing regions of rotational flow to exist in the solution. Viscous effects were modeled by coupling inviscid solvers with boundary layer methods.

Recently, several codes have been developed that solve the Navier-Stokes equations, the most accurate mathematical description of flow known to date. Yet, even these codes suffer from assumptions about the flow and computational weaknesses. Grids used to discretize the flow field are generally not fine enough to resolve all the details of a true flow. Current codes solve the Reynolds averaged form of the Navier-Stokes (N-S) equations, in which the effects of small scale turbulence are approximated by a turbulence model. Furthermore, artificial viscosity is required in order to achieve numerical convergence. Finally, due to computer limitations in both memory and CPU speed, most N-S high-lift studies are 2-D. Assuming 2-D flow, in turn, requires modeling assumptions to account for sweep, taper, and finite wing effects. Despite the limitations, these N-S methods provide the most complete viscous-flow analysis available.

The purpose of this study is to analyze the existing multi-element wing of the NASA Langley Transport Systems Research Vehicle (TSRV) using 2-D Navier-Stokes methods and correlate with wind tunnel and flight test data. Following this introduction is a brief review of multi-element airfoil flow issues in Section 2. Section 3 provides a description of the computational tools used in this study, along with 2-D test-case results. Section 3 ends with a description of the sweep theories which are applied to correlate with 3-D flight-test data. Section 4 provides a description of the flight experiment of the TSRV, which provides the basis of this study. Section 5 steps through the effects of surface

roughness, cove shape, sweep theory, grid refinement, and transition specification, leading up to the comparison with flight results. Next, the ability to predict the effects of changing free-stream conditions, in terms of angle of attack and Reynolds number are addressed. Finally, an analysis of the addition of Gurney flaps to the aft flap are shown. Section 6 summarizes the conclusions of this research. Throughout this text, various suggestions for future improvements will be made when appropriate.

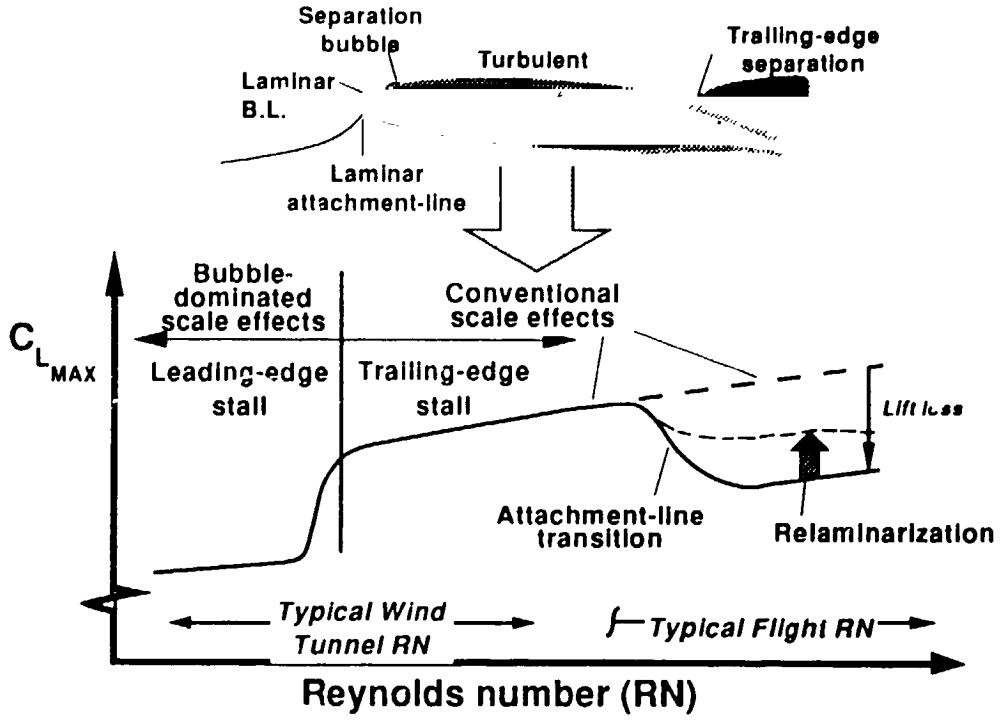

Figure 1.1 - Scale effects on maximum lift (From Reference 1).

2. Multi-Element Airfoil Flows

The effects of slots in multi-element airfoils were highly misunderstood before A.M.O. Smith's classic papers on high-lift aerodynamics[4,5]. Previously, the commonly accepted explanation for slotted airfoil performance enhancement was that the slot allowed high energy lower-surface flow to re-energize the upper surface boundary layer, thus delaying flow separation. On the contrary, Smith pointed out that slot flow is low in energy and the advantages of slotted airfoils involve mostly inviscid phenomena. Achieving improved high-lift performance requires understanding the boundary layer and separation, and finding the inviscid pressure distribution which produces the least stress on the boundary layer, thus reducing the tendency for flow separation.

As described by Smith, there are five predominant favorable effects of gaps in multi-element airfoil flows. The circulation of a forward element induces flow on a trailing element counter to the natural acceleration around the leading edge. This **slat effect** reduces the leading-edge suction peak on the trailing element, thus reducing pressure recovery demands and delaying separation. The trailing element, however, induces a **circulation effect** on the forward element which tends to increase the loading on the forward element, increasing the lift, but also increasing pressure recovery demands. Yet, the high velocity flow on the upper surface of the trailing element allows the flow to leave the forward element at a higher speed. This **dumping effect** reduces the pressure recovery of the forward element and favors **off the surface pressure recovery**, which is known to be more efficient than recovery in contact with a wall. Finally, each element has a **fresh boundary layer** which originates on

that element. A thin boundary layer can withstand stronger pressure gradients than a thick one and is less likely to separate. Effectively, the overall pressure recovery of the multi-element system is split by all the elements, but the boundary layer does not continuously grow along the chord as it would if the system was a single element.

The primary viscous effect of slots is the existence of individual wakes from each element of the system. These wakes are thought to provide a damping effect on the pressure peak of trailing elements, reducing the tendency of the flow to separate[3]. Yet, the wakes often tend to merge with the boundary layer of the trailing element. The resulting confluent boundary layer is much thicker than an ordinary boundary layer, so the likelihood of separation increases. Clearly, gap size optimization requires a balance between the inviscid and viscous effects which favor smaller and larger gaps, respectively.

3. Computational Methods

Multi-element flow solutions entail complex inviscid and viscous flow phenomena due to gap and cove structure and wake interactions. However, many conventional computational studies, particularly those used in design, use inviscid solution procedures with limited or no boundary layer modeling. While providing general insight into the flow development, such methods neglect many issues of importance, such as confluent boundary layers, cove flows and upper surface separation, and transition. While 3-D viscous grid generators and solvers are becoming available, current computational limitations, both in memory and CPU time preclude practical application. A logical compromise is a detailed 2-D viscous solution which requires computational power of the same order as 3-D inviscid solutions. The current study employs two currently available 2-D unstructured grid Navier-Stokes solvers.

3.1. Grid Generation

The flow field surrounding a multi-element airfoil is discretized with an unstructured grid consisting of triangular cells. This approach offers flexibility to conform to complex geometry and adapt to flow solutions. Cells are easily added where local refinement is needed to capture high gradients in the flow variables. Unfortunately, the lack of natural connectivity which gives unstructured grids such flexibility causes additional memory overhead. Alternative structured-grid approaches, such as the Chimera overset method[6] and the block structured approach[7] benefit from implicit connectivity within each zone, but suffer at interpolation interfaces and experience grid "striping" if adapted. Presently, no method is clearly superior and only the unstructured approach is discussed here.

With the objective of capturing viscous phenomena in the flow solution, the importance of grid topology cannot be overstated. In order to resolve the high gradients involved in shear flows, dense grid cell distribution is necessary. Yet, global refinement results in wasted memory and computation time in the areas where not needed. Thus, "efficient" grids utilize stretching factors to vary cell size between viscous and inviscid regions of the flow. Furthermore, viscous gradients commonly require much higher resolution in the normal direction than in the tangential direction. Figure 3.1 illustrates how high aspect ratio grid cells can be used to resolve viscous layers without an excessive number of nodes. While these high aspect ratio cells degrade the local efficiency and accuracy of the flow solver, the increase in global eifficiency justifies the use of such cells.

Two methods of unstructured grid generation were applied. The first is part of the NSU2D[8] package developed by Dimitri J. Mavriplis under the support of ICASE and McDonnell Douglas Aerospace. This method is designed to provide high aspect ratio viscous spacing near solid surfaces as well as in the wake regions in order to resolve boundary layer and wake flow structure. The other grid generation tool considered here is USVGRID[9] written by Shahyar Pirzadeh under the support of the NASA Langley Research Center. This method provides viscous type cells at solid surfaces and distributes cells smoothly around even the most complex shapes.

3.1.1. NSU2D package

Grid generation in the NSU2D package involves two primary steps: node generation, then triangulation. The point distribution comes from an interactive module called Gridpts. These nodes span the domain to be gridded, with coarse spacing in the outer region and fine spacing in the vicinity of airfoil surfaces. The output of Gridpts is triangulated in batch mode by UMESH2D. The topology of the resulting grid is largely determined by the point distribution

used for the triangulation.

3.1.1.1. Gridpts

The Gridpts module provides an interactive interface to distribute node points for the grid. The multi-element airfoil geometry is input. The user selects break points between which piecewise splines are fit to the geometry. A quick panel solution of flow past the configuration determines the approximate location of the wakes. The splined body shape and wake of each element forms an inner boundary for a structured C-mesh around that individual element. Normal spacing at the body, the number of points around the body, and the distance to the outer edge of the grid are among the inputs to the structured hyperbolic grid generator. The outer boundary of the main element structured grid will be the outer boundary of the final unstructured grid around the multi-element system. Note that up to this point, the process could be used for a Chimera overset grid method, but now we deviate.

The set of all nodes contained in the structured grids must be manipulated to provide a suitable point distribution for a single unstructured grid around the system. The structured grids are coarsened as desired to be used for multigrid convergence acceleration in the flow solver. Any points that fall within the body of any element are eliminated. Interactive sessions allow the specification of a "preserved region" around each element where the structure of the grid nodes is to be exactly preserved in the final triangulated grid. The final operations of Gridpts are a smoothing of the node distribution and removal of excess points. In particular, specification of a maximum cell aspect ratio and distance downstream to achieve it dictates the blending of viscous wake cells into the downstream region. Similarly, a maximum aspect ratio in the direction normal to the elements smoothes the inviscid point distribution.

Gridpts writes many intermediate files during the procedure. Thus, the

process may be interrupted and resumed at these intermediate points. Log files further expedite operation by providing user responses to various input needs (while preserving the interactivity of the graphic sessions). Log files are particularly helpful for the creation of multiple grids of varying coarseness, that are otherwise very similar, to be used with a multigrid algorithm or for a mesh refinement study. The final output file of Gridpts contains all the information needed in UMESH2D. It includes the set of nodes, the extent of the preserved regions, and stretching factors based on the aspect ratio distribution of the structured meshes.

3.1.1.2. UMESH2D

The points to be triangulated consist of two regions. The "inner region" incorporates the set of preserved structured grid regions around the elements. This region is triangulated simply by connecting a diagonal across each four-sided cell, so the original spacing is preserved. The "outer region" encompasses the rest of the domain and requires special treatment in order to achieve a smooth variation of cells from the high aspect ratio viscous region to the low aspect ratio inviscid region. The entire process is carried out in batch mode, guided by a small input file.

Triangulation of the outer region is accomplished using a Delaunay point insertion process[10]. The basic algorithm, credited to Bowyer[11], provides a method to systematically insert the desired node points into the triangulated region. The initial triangulation consists of cells extending from the inner to outer boundaries. As each point is inserted, all neighboring triangles with circumcircles that contain the new point are flagged. The edges of these existing triangles are removed and the resultant cavity region is re-triangulated by connecting the new node to every node along the edge of this cavity. The resulting mesh is a Delaunay triangulation of the given point set. This

construction has certain well-known properties, including a tendency to contain low aspect ratio cells. While acceptable for the inviscid region, this outer grid will not blend well with the high aspect ratio cells in the inner region, and abrupt changes in cell shape can be damaging to the solution. Thus, edge swapping operations revise the triangulation using the stretching vectors taken from the original structured meshes. The nodes are mapped to a stretched space for triangulation. When mapped back to physical space, the cells will flatten in proportion to the stretching factor, resulting in a smooth distribution of aspect ratio through the grid.

The resulting grid may be viewed using MESHPLT, which is available with the NSU2D package. Careful examination of the grid topology reduces the risk of failure in the solution process.

3.1.1.3. Limitations

While providing the means for generating excellent grids for viscous calculations, various limitations are addressed. As perhaps inferred in the preceding description, the process of generating grids using Gridpts and UMESH2D can be long and tedious, requiring several iterations before the desired topology is achieved (though log files partially relieve this effort). Typically, each iteration takes about fifteen minutes to perform, so generating a satisfactory grid may take on the order of a couple of hours. Also, the inherent ability of unstructured grids to fit any geometry is limited by the intermediate use of structured meshes in the process. Robustness problems arise in the structured grid generation, particularly in concave regions such as coves. To address this problem, the option to use alternative structured mesh generators is included in Gridpts. The value of the structured meshes in the process justifies the difficulties in their use. In addition to robustness problems in Gridpts, UMESH2D suffers from round-off errors in the point insertion process,

though these can usually be corrected by varying UMESH2D inputs. Another limitation of this process is the difficulty in achieving a smoothly blended mesh when long regions of high aspect ratio cells are retained in the wakes of the high-lift elements. Decreasing the extent of the viscous wake spacing smoothes the mesh but causes additional dissipation in the solution which reduces the ability to capture certain viscous interactions such as confluent boundary layers. Furthermore, generating smooth grids through thin gaps is difficult due to the preservation of structured mesh regions with high aspect ratio cells. Generally, as with any process, trade-offs must be made, and problems in grid generation with the NSU2D package can be averted with experience.

3.1.2. USVGRID

USVGRID provides a streamlined approach to unstructured grid generation. A single input file contains all the required information for the grid generation. USVGRID operates non-interactively with an optional graphical interface to view intermediate steps in the process, or can be run as a batch job. Euler grids, or Navier-Stokes grids with viscous spacing near the airfoil surfaces may be produced. Two common output formats are available so the grid may be used with a variety of available solution codes.

3.1.2.1. Operation

The primary hurdle in using USVGRID is preparation of the input file. A numbered list of points defines the surfaces of the airfoil geometry and outer boundaries. Piecewise splines through the given geometry points are indicated in lists of all the points composing each spline. Next is some information about the background mesh, followed by the locations and strengths of "sources" which govern the size and clustering of the cells in the mesh. The region of influence for each source is also specified. Finally, for viscous grids, the normal

spacing at the body and a stretching factor to control the rate of decrease of cell aspect ratio in the normal direction are listed.

The generation of viscous grids with USVGRID is accomplished with an Advancing Layer/Advancing Front approach[9]. The grid cells are created as the front marches outward from the inner boundaries. The viscous grid for the region near solid surfaces is generated by the Advancing Layer technique in which nodes are added along lines normal to the surface using the specified spacing and stretching. Beyond a certain distance from the surface, the Advancing Front technique is used to provide an isotropic triangulation of the remaining inviscid region. Grid "shocks"[12], which typically occur in structured grids near concave corners, are avoided in this unstructured approach by a test procedure which predicts when cells in the current march will overlap and reduces the number of new faces on the next front accordingly. The entire grid generation process is rapid, one iteration taking about five minutes. The resulting grid is very smooth, generally with more gradual variation in cell size through the mesh than in grids generated with UMESH2D.

3.1.2.2. Limitations

The primary difficulties involved in USVGRID are associated with the complex input file. Specification of the spline lists and source terms will be much simpler when a graphical interface for interactive specification becomes available; such an interface is under development. Until available, use of a pre-processing code is prudent. Placement and properties of source terms require several levels of iteration until the desired node distribution, particularly near the solid boundaries, is achieved. Then, when the desired resolution is obtained near the airfoils, the grid tends to have excess nodes away from the airfoils and will require more computation time in the solver. Also, no high aspect ratio cells are generated downstream of the elements for fine resolution

of wakes and confluence. Perhaps an option could be to define a wake line along with the geometry from which to march cells initially using the advancing layers approach used on the element surfaces.

3.2. Mesh Adaptive Refinement

Considering the influence of grid topology on the flow solution, the ability to refine existing grids to better suit a particular solution is considered. As mentioned previously, local refinement to capture high gradients is more efficient than global refinement. The unstructured grid generation process distributes cells with refinement where the need is expected. However, without *a priori* knowledge of the solution, the grid will likely lack the needed resolution in some areas of the flow. For instance, wakes will dissipate where the grid is too coarse, so the occurrence and effects of confluent boundary layers cannot be addressed. Furthermore, wake locations change in different operating conditions, so grid clustering may not exist where needed. Also, failure to accurately predict pressure peaks can lead to entropy generation and other globally damaging effects in the solution. The motivation for solution-adaptive refinement is the ability to selectively add nodes only in regions where gradients in the flow variables are large. The refined mesh either replaces the existing mesh for a new calculation or may be added to the top of a multi-grid sequence.

3.2.1. NSU2D Adaptive Refinement

The NSU2D package includes MESHAD for solution-adapted grid refinement. MESHAD uses the geometry spline information (an intermediate Gridpts file), the existing finest grid, and a restart file from the NSU2D solver to generate a new grid. In the MESHAD input file, each flow variable to be examined and the criterion for adding nodes is specified. The flow variables available for adaptation are density, pressure, velocity magnitude, and Mach number. Resolution of inviscid phenomena, such as pressure peaks can be

achieved using density or pressure, whereas high Mach number and velocity gradients occur in regions of viscous shear flow. Any combination of these variables may be used. The criterion for refinement to a particular property is the ratio of the local change in that property within one cell to the average change within all cells in the domain. The allowable ratio is specified in the input file, and any cell that exceeds this ratio has new points added at the midpoints between the existing nodes. Specifying the ratio as 0 results in global refinement, producing four times as many cells in the grid, and a ratio of 1 results in refinement anywhere the gradient is higher than average. Once all new points are determined, they are added to the existing mesh using the point insertion prccess as in UMESH2D.

3.2.2. USVGRID

No solution-adapted refinement code is currently available for use with USVGRID (partially attributed to the fact that development of USVGRID is independent of a particular solution code). Manual refinement can be accomplished by viewing a solution and adjusting the source placement and strengths in the input file and generating a new grid better suited to the solution.

3.3. Navier-Stokes Solvers

The full Navier-Stokes equations provide a complete mathematical model for flow solutions. However, computational limitations in both hardware and software require assumptions to simplify the process. In order to reduce computer processing and memory requirements, 2-D flow is studied here. Still, the length scale of turbulent phenomena is generally smaller than the cell size of current grids, so the equations are Reynolds averaged and the mean effects of the small scale turbulence are accounted for by a turbulence model. The purity of the mathematical model is further compromised by the requirement of numerical stability, which is achieved by adding artificial viscosity to the

equations[13]. Available solvers are utilized in this study, but the understanding of the solution is incomplete without knowledge of the assumptions and limitations in the formulation.

3.3.1. Governing Equations

The Reynolds-averaged Navier-Stokes Equations govern the continuity of mass, momentum, and energy, and are given as:

$$\frac{\partial w}{\partial t} + \vec{\nabla} \cdot \vec{F}_c = \frac{1}{\mathrm{Re}_\infty} \vec{\nabla} \cdot \vec{F}_v \tag{3-1}$$

where Re_∞ is the free-stream Reynolds number based on the free-stream velocity, U_∞ and the reference chord, c, and w is the set of conserved variables:

$$w = \begin{bmatrix} \rho \\ \rho u \\ \rho v \\ \rho E \end{bmatrix} \tag{3-2}$$

with density, ρ, velocity, $\vec{U} = u\hat{i} + v\hat{j}$, and total energy, E. The convective fluxes, $\vec{F}_c$, consist of algebraic functions of the conserved variables and the pressure, which is related to the conserved variables through the equation of state for a perfect gas. The viscous fluxes, $\vec{F}_v$, consist of functions of the first derivatives of the velocity components, as well as molecular viscosity, μ, and turbulent eddy viscosity, μ_t. (For details, consult References 8, 19). Sutherland's Law may be used to compute μ, but μ_t must be solved for simultaneously with the conservation relations using the additional equation(s) provided by a turbulence model. In this formulation, the global effects of small scale turbulence are imposed on the solution without requiring the extreme grid resolution which would otherwise be necessary to capture the full turbulence effects. Consequently, the quality of the solution depends on the ability of the turbulence model to accurately predict turbulence levels which contribute to the

viscous stress and heat flux in the flow. The turbulence model used in this study is the one-equation model of Spalart and Allmaras[14], which has been found to provide better results than many alternative models[15,16].

3.3.2. NSU2D

The steady-state flow solution is calculated by NSU2D using an explicit Runge-Kutta time stepping scheme applied to a finite element discretization[8]. Convective terms are central differenced and two forms of artificial viscosity are used: second-order accurate biharmonic operators throughout the domain, and first-order accurate Laplacian terms in regions of high gradients or shocks. As with any explicit scheme, the time step used is limited by a stability condition known as the CFL number, named after Courant, Friedrichs, and Lewy[13]. The exact form of the CFL number depends on the discretization, but is generally of the form: $CFL = \left| c \frac{\Delta t}{\Delta x} \right|$, with CFL typically less than 1 for stability of a single-stage explicit scheme. The five-stage Runge-Kutta integration scheme applied in NSU2D allows the use of CFL numbers up to around 3.5[17].

Since most studies concentrate on the steady state solution and not the transient, the definition of "time" is relaxed, allowing various methods of convergence acceleration to be used. A simple method is to observe the dependence of a stable time step on the cell size and thus allow the time step to vary throughout the mesh. In addition to local time stepping, residual smoothing can further accelerate convergence. By implicitly averaging residuals with those of neighboring nodes, the stability limit of the scheme increases, allowing the use of larger CFL numbers. A CFL number of 5 was found to provide a good balance between efficiency and robustness.

Another more recently developed and more powerful convergence acceleration technique is multi-gridding[18]. Solutions rapidly obtained on sequentially coarser grids provide improved corrections for the fine grid, on

which detail in the flow solution is obtained. Typical multigrid cycles are illustrated in Figure 3.2. The larger cells of the coarse meshes allow more rapid travel of boundary information, as well as damping out high frequency noise in the solution. Independent triangular meshes make up the multigrid sequence rather than using subset coarsened meshes or polyhedral agglomeration[19] techniques, allowing control over grid topology and allowing arbitrarily refined meshes. The transfer of information between meshes is accomplished by a simple linear interpolation between the node of one mesh and the nodes of the surrounding cell on the other mesh. This information is stored as 3 interpolation addresses and 3 weights for each node, as determined in a pre-processing operation.

Operation of NSU2D involves a primary input file which provides details for the solution process, along with the names of the grid files and if any laminar flow regions are to be specified, a boundary-layer transition file. The flow solver may be compiled and run on a supercomputer or a workstation if sufficient memory is available. Typically between 10 to 20 Mwords of RAM on a Cray, or from 64 to 96 Mbytes of RAM on a workstation are needed for the computations, depending on the grid size. Upon completion, a restart file containing all the flow variables at the current time step is written, allowing the job to be re-submitted if further convergence is desired. The solution for the entire flow field is written to a file which may be viewed using PLOT2D, which is available with NSU2D. The finest grid, contours of various flow properties, and velocity vectors may be viewed. A post-processing operation may be used to extract velocity profiles comparable to boundary layer rakes used in experimental studies. Another file contains convergence information and surface values which may be post-processed to plot surface properties such as pressure coefficient.

3.3.3. FUN2D

FUN2D was developed at NASA/Langley Research Center by W. Kyle Anderson[20]. An implicit, upwind finite element scheme is used to march the solution to steady state. The implicit formulation provides numerical stability, allowing higher CFL numbers, and thus larger time steps, to be used. FUN2D is stable using a CFL number on the order of 100, as compared to around 5 for NSU2D. The apparent gain in speed is balanced by the longer time per iteration than the explicit scheme due to the need for solving a large simultaneous system of algebraic equations at each time level, resulting in comparable times for numerical convergence between the codes. Artificial viscosity is not explicitly added in the equations, but the stabilizing effect is provided by the upwinding of the convective terms in the equations (See Appendix 1). Convergence acceleration techniques such as multigridding and local time stepping are implemented as in NSU2D.

Operation of FUN2D is much like that of NSU2D, including a restart option and comparable output files. The output is formatted for use with the FLANAL visualization package developed by Kelvin Edwards at NASA/Langley Research Center. As will be shown in the following section, the results of NSU2D and FUN2D are in good agreement for a three-element configuration, as they are for all configurations studied. Thus, only a brief comparison between solvers is conducted, and most solutions are obtained using NSU2D.

3.4. 2-D Test Cases

Before discussing 3-D flow fields, an evaluation of the numerical methods using strictly 2-D test cases is advantageous. Computational results include error introduced by the formulation, discretization, and computer round-off. In addition, the correlation with 3-D data involves error due to sweep corrections, as well as the lack of spanwise flow, interference, and wing-tip

effects in the 2-D calculations. Furthermore, actual aircraft used in flight exhibit more of a tendency to deform aeroelastically than wind-tunnel models. Thus, comparison with 2-D wind-tunnel data greatly reduces the sources of potential error and allows an objective evaluation of the capability of the codes.

The Low Turbulence Pressure Tunnel (LTPT) at NASA Langley provides an abundance of reliable test data including several tests of multi-element wing sections at Reynolds numbers approaching those of flight. The first case considered here is a three-element airfoil available from McDonnell Douglas Aerospace which was used as a benchmark test case in the High-Litt Workshop at NASA Langley in May 1993[21]. The second is a four-element airfoil developed by the Boeing Commercial Airplane Group. The geometry of this configuration remains proprietary.

3.4.1. Three Element

The three-element airfoil tested is McDonnell Douglas model MDA LB-546, which consists of a slat, main element, and a flap. The particular case used for this comparison is Geometry A of the High Lift Workshop, which is a landing type configuration with a 30° flap deflection. Free-stream conditions are characterized by a Mach number of 0.20, Reynolds number of 5 million, and angle of attack of 8.12°. A typical grid used for the calculation is shown in Figure 3.3. This grid contains 48121 nodes, with 291 nodes on the main element surface, 319 nodes on the slat, and 265 nodes on the flap. Two coarser grids, each with about one fourth as many nodes as the previous, are used for the multi-grid sequence. The NSU2D solution requires about 8.5 Mwords of memory and 30 minutes of CPU time on a single processor of a Cray Y-MP supercomputer. FUN2D requires about 28 Mwords of memory and 25 minutes of single-processor Cray Y-MP time. The required memory per node is approximately 180 words/node for NSU2D and about 600 words/node

for FUN2D. On an IRIS Indigo 2 workstation, using double precision, an NSU2D solution requires around 64 Mbytes of memory and on the order of 10 hours of CPU time. The convergence histories for NSU2D and FUN2D are shown in Figures 3.4 and 3.5, respectively. Both plots show the decrease of a local quantity, namely the maximum rate of change of density or mass, and the asymptotic convergence of a global quantity, the lift coefficient. For both codes, a four order of magnitude reduction in the residual, and a convergence of the lift coefficient to the fourth decimal place is accomplished within one hour of Cray CPU time for all grids tested.

The surface pressure distribution is well predicted by both codes, which are in close agreement, as shown in Figure 3.6. The overprediction of the slat pressure may be due to poor representation of the separated cove flow due to limitations of the turbulence model, resulting in increased circulation on the element. The overprediction of the main element pressure peak may also contribute to the overprediction of the slat loading through the circulation effect. The flap pressure comparison is very good. As previously mentioned, since NSU2D and FUN2D give very close to the same results, no further comparisons between the two codes are shown.

While the surface pressure comparison shown here resembles the state of the art seen at the workshop and in the literature, the ability to better capture the flow structure is addressed with a grid resolution study. The grid presented above is used as the baseline case. A coarse grid comparison simply uses a solution obtained on the next grid of the multigrid sequence used in the baseline case. A finer mesh was also generated to test grid dependence, and was also designed to include long regions of high aspect ratio cells in the wake region of each element in order to discern the value of including such cells. The sizes of the three meshes are listed in Table 3.1.

	Baseline Mesh	Coarse mesh	Fine Mesh
Total Nodes	48,121	12,173	70,720
Slat Surface	319	160	299
Main Element Surface	291	147	379
Flap Surface	265	133	299

Table 3.1 - Mesh sizes for three-element grid comparisons.

The computed surface pressure distributions for the three mesh cases are shown in Figure 3.7. Perhaps even more revealing are boundary-layer profiles, which are shown in Figure 3.8. The experimental profiles were taken using a boundary-layer traverser. The computational results are found by computing a surface normal at each chordwise station desired and taking the component of velocity perpendicular to this line by interpolating between nodes of the grid. The coarse mesh clearly has normal spacing near the surface which is too large to resolve the boundary layers. The artificially thick boundary layers and wakes tend to dampen the pressures on trailing elements and thus reduce the circulation of the entire system. The pressure prediction of the baseline and fine mesh are very similar, suggesting that the baseline mesh is adequate for general solutions and the additional high aspect ratio cells carried into the wake are not necessary for prediction of the pressures.

The velocity profiles are also very similar for the baseline- and fine-mesh solutions, both resolving wakes much better than the coarse-mesh solution. The extended region of high aspect ratio cells in the fine grid does reduce wake thickness slightly and improves the velocity levels. The fine grid solution shows a slat wake at the $\eta = 0.45$ station. The experimental result has only a slight perturbation at this location, but the experimental slat wake may have been

disturbed by the instrumentation and tunnel turbulence, and should be somewhat thinner than the fully-turbulent computations which do not include any laminar flow on the slat. Dissipation in the computational solutions due to cell size and artificial viscosity is evidenced by the spreading of the wake as it convects downstream. With the coarse grid, the slat- and main-element wakes completely dissapear within a short distance downstream. Near the trailing edge of the flap (η = 1.122), there is a discrepancy between computation and experiment on the location of the wake center. The incipient separation in the experimental profile is not predicted in the computations, suggesting the need for further development of turbulence models. The multi-element flow structure is best resolved with fine grid spacing in the wake regions, so the calculations in this study are made using grids generated with the NSU2D package rather than USVGRID.

3.4.2. Four Element

While the three-element results show excellent agreement between computations and experimental data, several issues remain to be addressed before comparison with the five-element results of the TSRV. First, the accuracy of the codes may degrade as the flow field becomes more complicated by the addition of lifting-surface elements. Also, the interaction of multiple flap elements in close proximity is of interest. In particular, the four-element airfoil analyzed here includes a small vane element followed by the main flap element, not unlike the first two flap elements of the TSRV airfoil section. Because this geometry is a current interest of the Boeing Commercial Airplane Group, the geometry and results are not being published, so only a discussion of the results are included here.

The solution was run for a flap setting appropriate for landing, at 5.9° angle of attack, a Mach number of 0.18, and three Reynolds numbers: 2.45-,

6.70-, and 15.97-million. The finest grid for the solution contains 71812 nodes, with 253 nodes on the slat element surface, 371 nodes on the main element, 301 nodes on the vane, and 299 nodes on the flap. The computational results from NSU2D and FUN2D closely match those of the wind-tunnel experiment. The computations also accurately predict the variation with Reynolds number. Both codes predict the rise in the leading-edge pressure peaks with Reynolds number, and the levels are accurate. There is a slight discrepancy in the slope of the pressure recovery near the flap trailing edge for the two higher Reynolds numbers. This discrepancy may be attributed to inaccuracies in the turbulence modeling in regions with high Reynolds stress, although no upper surface separation was evident. Overall, however, the results of this test case illustrate the ability of these codes to accurately predict the flow field and Reynolds-number effects for complicated 2-D multi-element configurations.

3.5. 2-D to 3-D Correlation

In order to apply 2-D methods to the study of aircraft wings, an understanding of the influences of 3-D effects on the flow is necessary. This study involves a 2-D analysis of an existing multi-element wing and correlation with flight-test data. In order to compare with the flight results, the effects of downwash, sweep, and taper on the 2-D solution must be accounted for. Currently, no method provides all 3-D factors short of a full 3-D solution, which is currently infeasible due to computer limitations (as discussed previously).

The most basic method is known as a simple-sweep correction[22]. This is easily accomplished in pre- and post-processing operations, so modification of existing 2-D codes is not necessary. Simple-sweep theory is purely geometric, as illustrated in Fig 3.9. Applying simple sweep theory entails choosing a 2-D section of the wing in the freestream direction and rotating the cut by some nominal angle of sweep so the section is in a normal chordwise direction.

Then, the 2-D solution is found and the results are corrected back to the free-stream direction. Only the effect of sweep is accounted for, so this correction is only rigorously valid for an infinite-span, untapered, swept wing.

In the pre-processing operation, the airfoil shape is modified by preserving a non-dimensional chord length so x/c is unchanged, and altering the y-values of the surface coordinates as:

$$\frac{y}{c_n} = \left(\frac{y}{c}\right)\left(\frac{c}{c_n}\right) = \frac{\left(\frac{y}{c}\right)}{\cos\Lambda}, \tag{3-3}$$

resulting in a thicker airfoil section (In reality, the thickness is unchanged and the chord is smaller). The components of the free-stream Mach number and Reynolds number in the normal direction are also found from the geometry:

$$M_n = M_\infty \cos\Lambda, \tag{3-4}$$

$$\mathrm{Re}_n = \frac{U_n c_n}{\upsilon} = \frac{(U\cos\Lambda)(c\cos\Lambda)}{\upsilon} = \mathrm{Re}_\infty \cos^2\Lambda. \tag{3-5}$$

The 2-D solution is found for the modified section using M_n and Re_n. Typical qualitative outputs such as the velocity vectors and pressure contours around the system are viewed in un-corrected form. Yet, any features that are to be directly compared with flight results must be converted back to the streamwise direction for comparison. Namely the surface Cp distribution, and any values of forces, such as the normal force, lift, and drag which were calculated before the sweep correction, must be "unswept". The procedure for correcting Cp begins with the calculation from the 2-D solution at each chordwise location, i:

$$Cp_{n_i} = \frac{P_i - P_\infty}{\frac{1}{2}\gamma P_\infty M_n^2} \tag{3-6}$$

Yet, we want Cp relative to the free-stream direction:

$$Cp_i = \frac{P_i - P_\infty}{\frac{1}{2}\gamma P_\infty M_\infty^2} \tag{3-7}$$

and this is achieved by multiplying Eq. (3-6) by the square of the ratio of the normal Mach number to the free-stream Mach number:

$$Cp_i = \frac{P_i - P_\infty}{\frac{1}{2}\gamma P_\infty M_n^2}\left(\frac{M_n}{M_\infty}\right)^2 = Cp_{n_i}\left(\frac{M_n}{M_\infty}\right)^2 \tag{3-8}$$

and applying Eq. (3-4), this yields:

$$Cp_i = Cp_{n_i}\cos^2\Lambda\,. \tag{3-9}$$

In addition to the simple-sweep rule, the correlation with flight data requires an angle of attack correction to account for the 3-D finite wing effect. Because the true wing has a finite span, wing-tip vortices and the associated downwash alter the direction of the effective incoming flow past the section. Unfortunately, the induced angle of attack is not known in general for the wing section, so the choice of α_n used in the 2-D computation is somewhat arbitrary and requires iteration. One method commonly used in conjunction with experiment is to choose α_n such that the section Cn matches that of experiment. However, this criterion is believed to be excessively optimistic, and the Cp distribution will certainly be close since the pressure integration yields the same normal force coefficient, Cn. The method of finding α_n used in this study is to choose that for which the slat element upper surface pressure distribution most closely matches the experimental level. The lead element is least likely to be affected by viscous effects due to its fresh, thin boundary layer and position upstream of the wakes of other elements. Using this downwash correction, the computational inaccuracies in the downstream flow and in the prediction of forces on the system can more realistically be assessed.

While simple sweep theory is easily implemented and provides relatively

good comparison with flight[23], it is subject to several limitations. One improvement to the simple-sweep theory is accomplished by accounting for wing taper. Rather than using a single nominal sweep angle for the 2-D to 3-D conversion, a local sweep angle is calculated for each chordwise station, i. Thus, the new y-values are calculated from:

$$\frac{y}{c_n} = \left(\frac{y}{c}\right)\left(\frac{c}{c_n}\right) = \frac{\left(\frac{y}{c}\right)}{\cos\Lambda_i}, \tag{3-11}$$

Note that the only difference with the simple-sweep correction in Eq. (3-3) is that here the sweep angle, Λ_i, varies along the chord. The chordwise variation in sweep angle is linear in the tangent, as derived in Appendix 2. Thus, the 2-D geometry comes from a circular arc cut through the wing rather than a straight line, as sketched in Figure 3.10. Similarly, the Cp correction uses the local sweep, Λ_i.

Based on the theory and knowledge of the wing being studied, some predictions about the local sweep rule results may be made. First, because the sweep angles are more accurate, the flow prediction should be more accurate. However, flap loadings tend to be overpredicted due to "blow-back" in flight and other geometrically-related errors, as well as grid resolution and computational errors. (Blow-back refers to the movement of the airfoil elements when loaded due to "play" in the flap linkages, reducing flap incidence angles and gaps.) Because the wing taper ratio is less than unity, and the wing sweep is rearward, the flap sweep angles are less than the nominal quarter chord sweep used in the simple sweep approach. Thus, from Eq. (3-9), we see that the error in tne simple sweep method will result in decreased Cp values over the flap elements compared to the local sweep approach, making simple sweep appear to correlate better with flight for the flap elements.

A third method of sweep correction is based on the empirical results of

the British "National High Lift Programme" reported by D. S. Woodward and D. E. Lean in Reference 24, and is implemented here as an addition to the local sweep procedure. In Reference 24, comparisons between wind tunnel results obtained with 2-D airfoils and wind tunnel results obtained with swept semispan wings revealed a consistent alteration to the Cp correction, of the form:

$$Cp_i = Cp_n \cos^n \Lambda, \tag{3-12}$$

Rather than applying the exponent, n = 2, which is purely geometric, n was allowed to vary in the chordwise direction. The best correlation between 2-D and 3-D test data was found to use the exponent, n = 1.1 on the slat element, n = 2.1 on the main element, and n = 3.6 on the flaps. The explanation for this variation in the value of the exponent is unknown. Yet the fact that the exponent n is near 2 for the main element agrees with the geometric theory. Perhaps the modification for the slat and flap elements partially accounts for the chordwise variation in downwash from the tip vortices of the 3-D model, which was observed in Reference 24. The higher downwash in the vicinity of flap elements decreases the effective angles of attack, thus reducing the loading. Since $\cos\Lambda < 1$, the higher value of the exponent, n, for the flap elements will decrease the computed pressures of the 2-D solution, which will better match the 3-D pressures. Likewise, the smaller value of the exponent, n, for the slat will reduce the extent of the decrease of the pressure on the slat due to the sweep correction and will thus increase the α_n for the correlation.

It should be mentioned that application of a different sweep correction requires more than simply altering the numbers in pre- and post-processing operations. Since the geometry depends on the sweep rule, the entire computation process, including the generation of new grids, must be repeated for each new sweep correction.

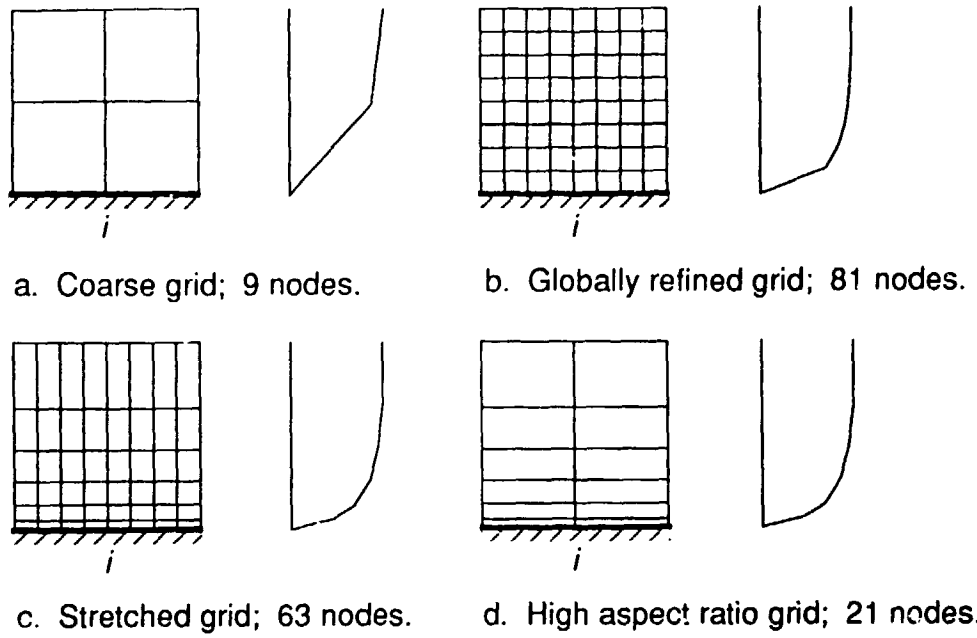

a. Coarse grid; 9 nodes.

b. Globally refined grid; 81 nodes.

c. Stretched grid; 63 nodes.

d. High aspect ratio grid; 21 nodes.

Figure 3.1 - Grid topology at solid surface and typical velocity profile at *i*.

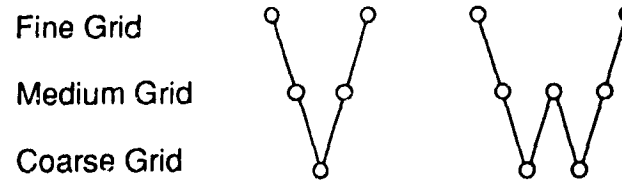

a. V-Cycle

b. W-Cycle

Figure 3.2 - Typical multigrid cycles.

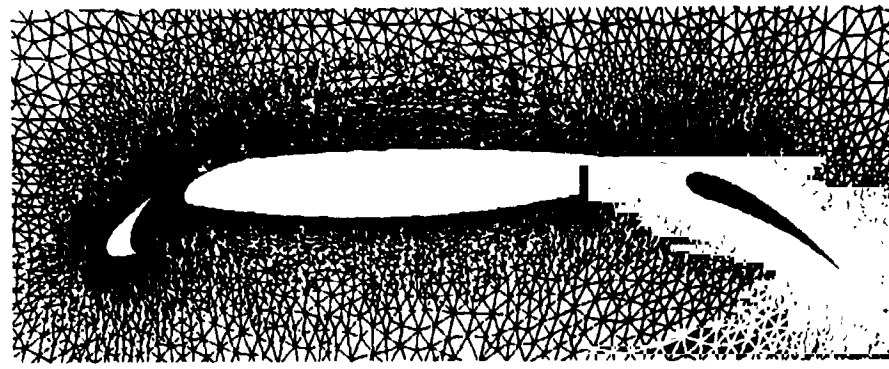

Figure 3.3 - Typical grid for three-element airfoil computations.

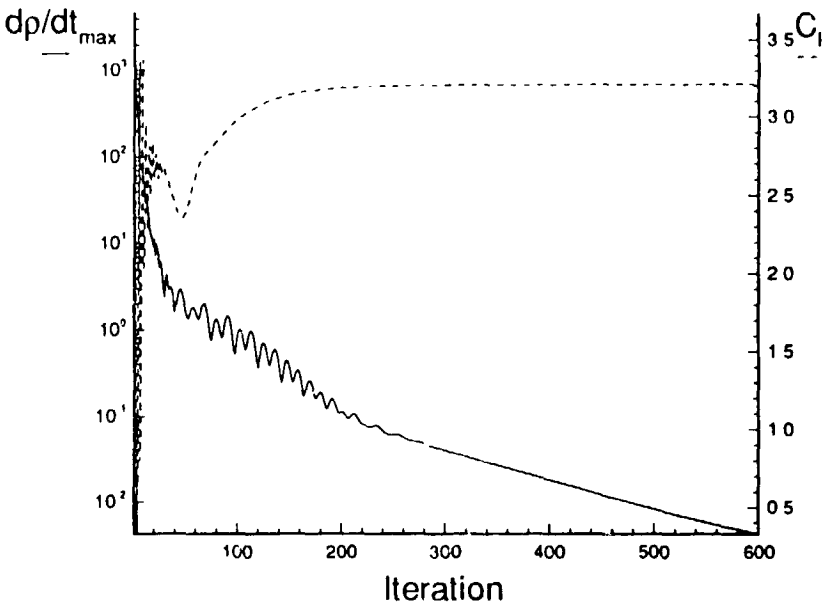

Figure 3.4 - Typical convergence history for an NSU2D solution.

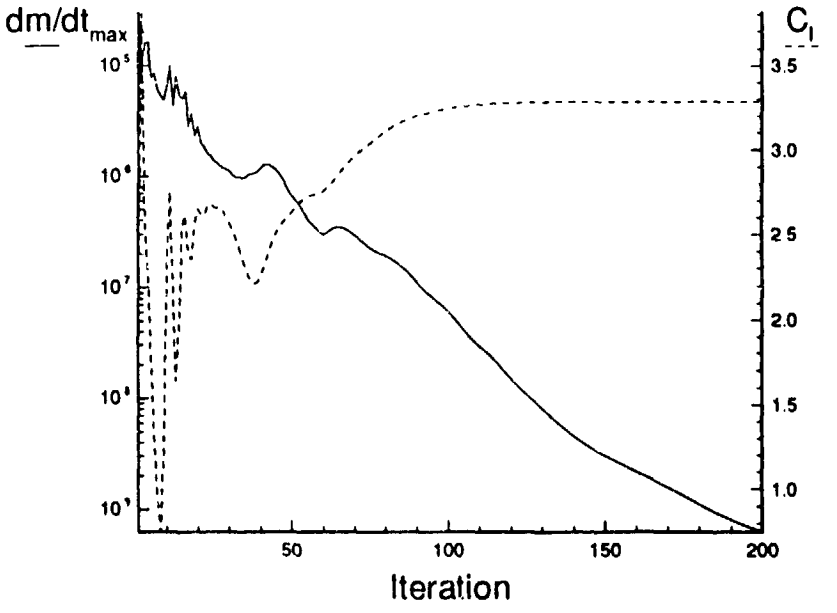

Figure 3.5 - Typical convergence history for a FUN2D solution.

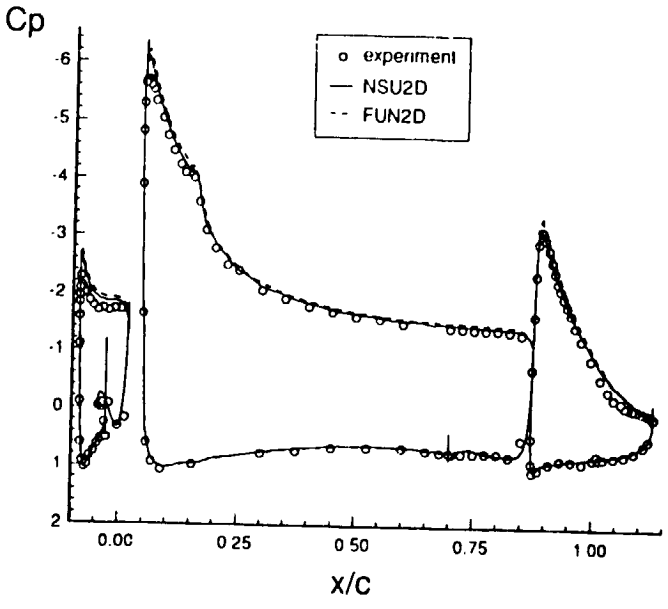

Figure 3.6 - Comparison between experimental and computed pressure distributions for a three-element airfoil. (M = 0.20, Re = 5 million, α = 8.12°)

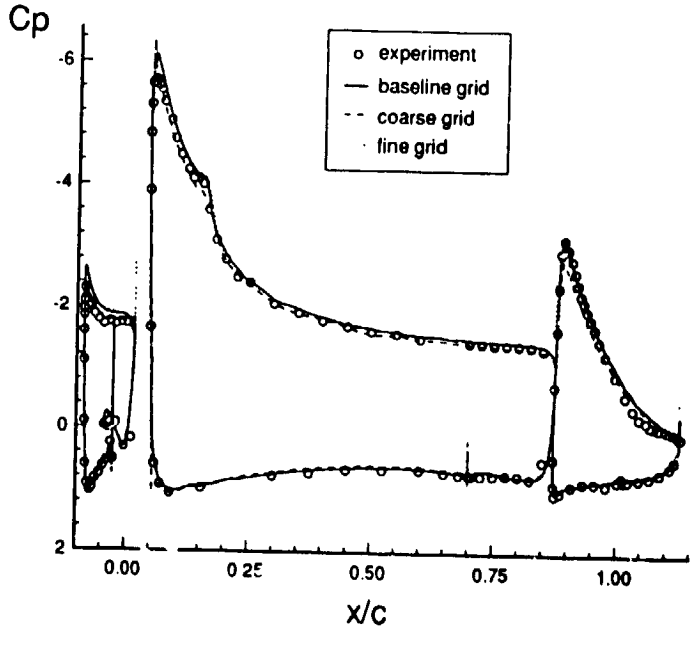

Figure 3.7 - Effect of grid topology on predicted pressure distribution.

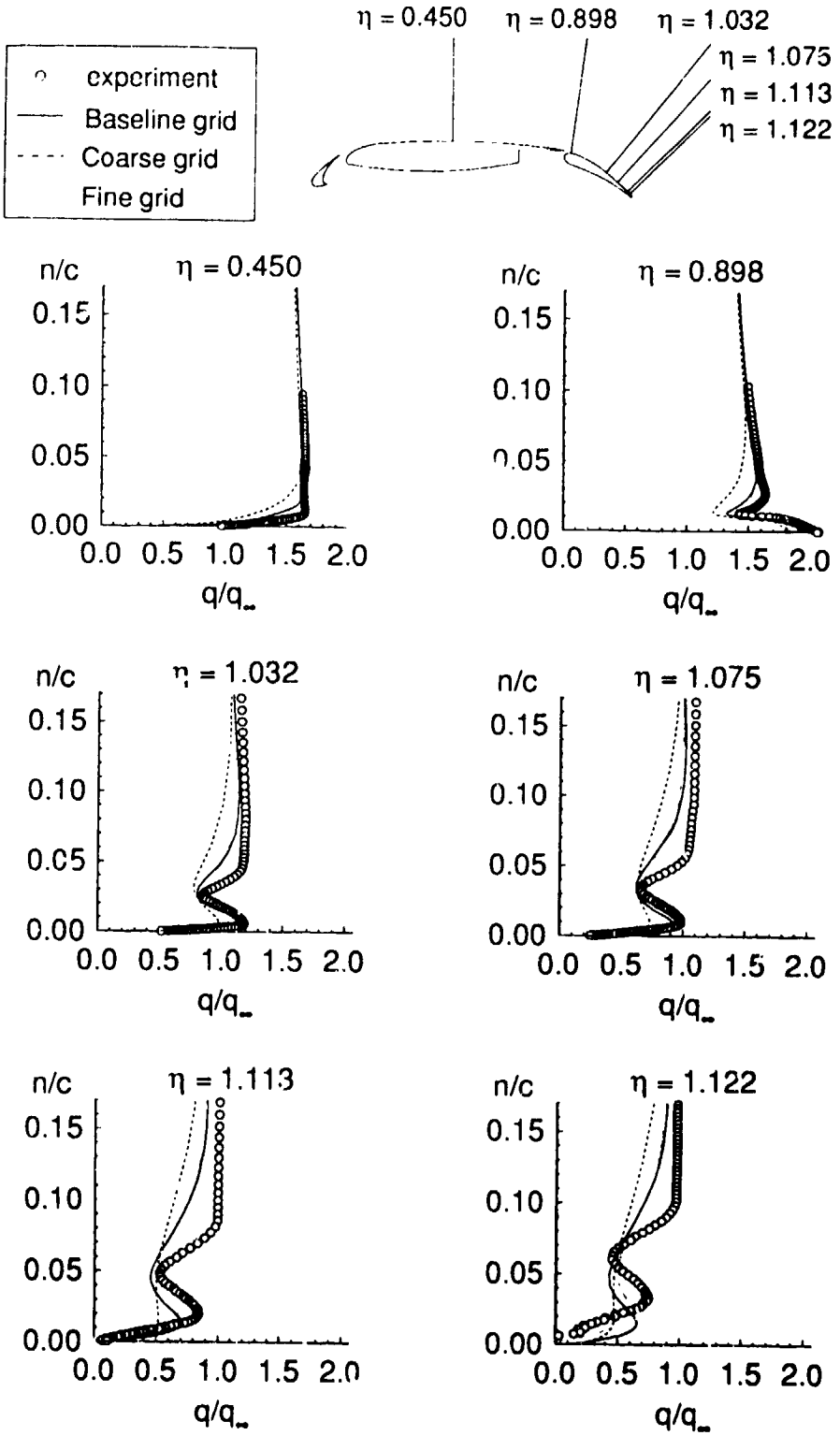

Figure 3.8 - Effect of grid topology on boundary-layer velocity profiles.

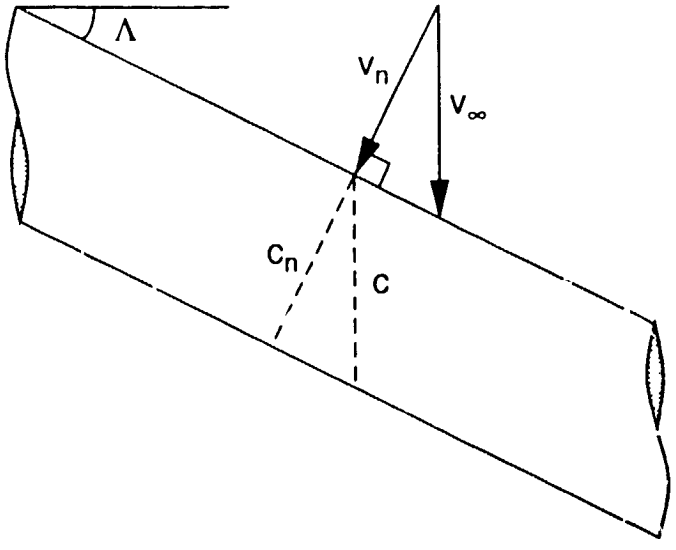

Figure 3.9 - Simple-sweep relations for an infinite aspect ratio, untapered, swept wing.

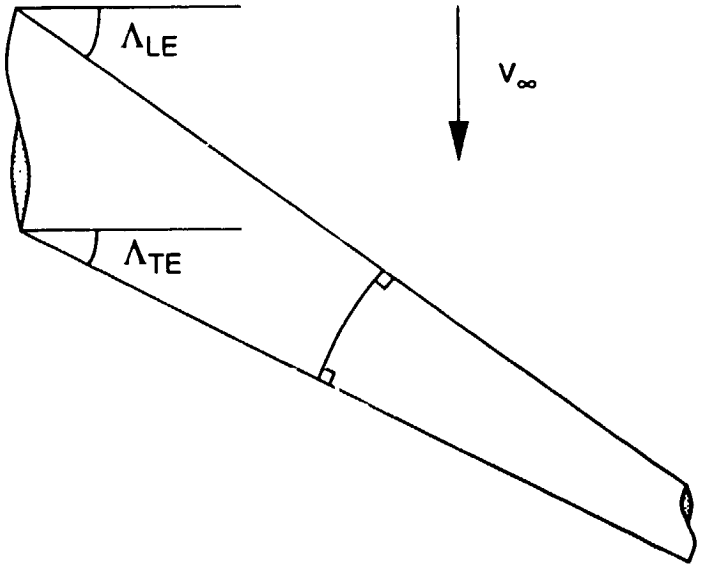

Figure 3.10 - Local-sweep theory; effective cut through an "infinite" aspect ratio, tapered, swept wing.

4. Description of Flight Experiment

The Transport Systems Research Vehicle (TSRV) is the prototype B737-100 which has been highly modified for high-lift flight research. This aircraft, shown in Figure 4.1, provides a good representation of typical transport systems in terms of size and planform, while the five-element airfoil provides a challenge for analysis methods and CFD code validation. Although future designs will likely involve less geometric complexity, the basic elements of multi-element flow physics are well represented by this test case. Test results indicate the existence of flow separation, attachment-line transition, boundary-layer relaminarization, and likely confluent boundary layers.

The Phase I and II flight tests included a limited array of instrumentation to provide some preliminary insight into the flow, and key results were presented in Reference 1. Pressure belts around each element at the 58% semispan station provided the chordwise load distribution. When flaps are deployed, these belts are not all at the same spanwise station, as shown in Figure 4.2, but the effect on the results is thought to be minor. Preston tubes placed on the main element upper- and lower- surfaces and the slat upper surface provided insight into the skin friction on the wing. The test matrix included a range of angle of attack for three pressure altitudes, five-, ten- and twenty-thousand feet.

The upcoming Phase III flight tests scheduled for Spring, 1994 will include a more complete array of instrumentation to help answer many questions which have arisen in both the Phase I and II analysis and the current computational effort. Flush pressure ports will address the effect of pressure belts on the measurements. The pressure will be measured at five spanwise

stations to test the two-dimensionality of the flow near the half semispan. A boundary-layer rake on each element will show boundary layer thickness, separation, and confluence. The Northern Digital OPTOTRAK[25] system will reveal in-flight deflections due to blowback and aeroelastic deformations, helping to reduce geometry-related error in the analysis. Hot films will provide more detailed illustration of the boundary layer state. Finally, Gurney flaps of 1% and 2% lengths will be tested. Decisions on the placement and sizing of the instrumentation were based on Phase I and II test results as well as preliminary computations.

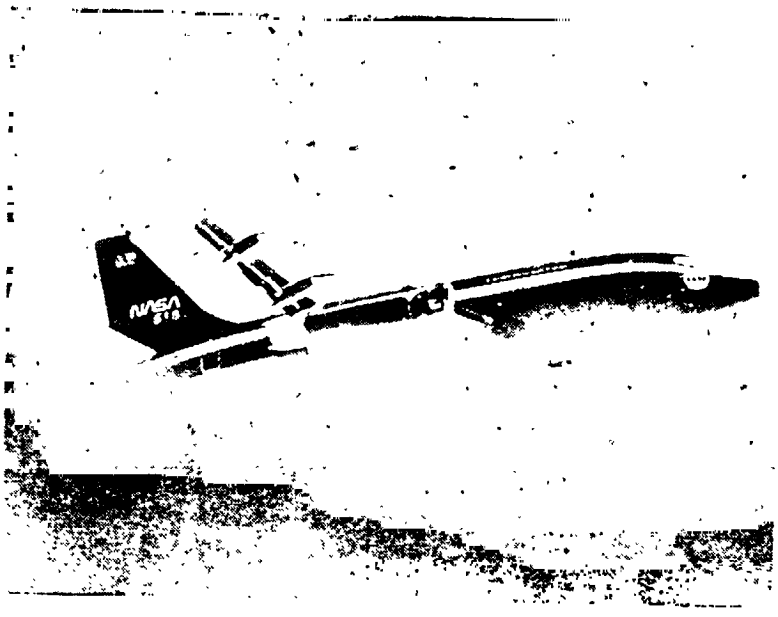

Figure 4.1 - NASA Langley TSRV test aircraft (B737-100).

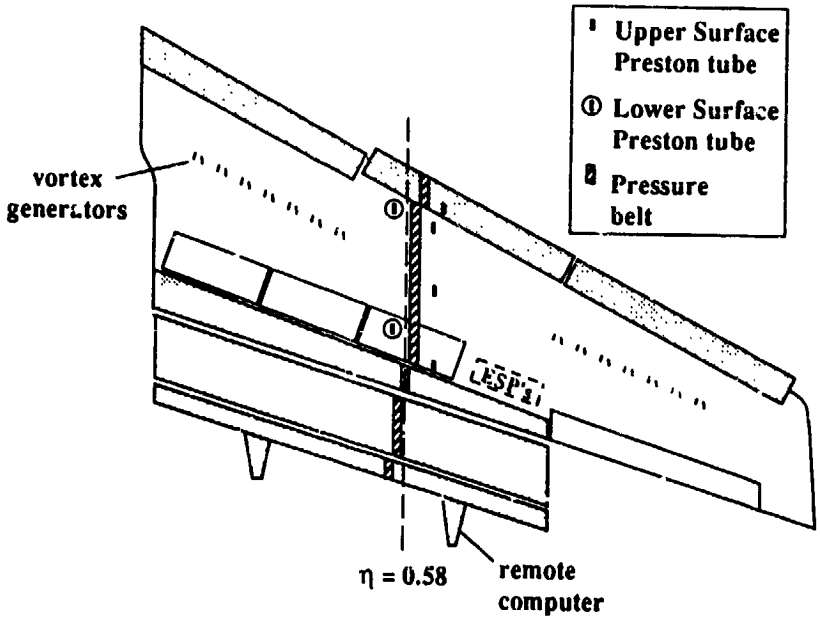

Figure 4.2 - Phase II flight test instrumentation layout.

5. TSRV Results

The computational analysis of the TSRV wing section provides a means for evaluation of the capability of the current codes and sweep theories. The use of an actual aircraft wing and correlation with flight data reveal numerous difficulties encountered in a design environment which do not arise when comparing to 2-D wind tunnel data. In the following sections, various issues in the process leading up to the correlation with flight test results are addressed.

A typical primary mesh for the five-element computations is shown in Figure 5.1. The spacing on the element surfaces and the distribution of nodes in the flow field is based on the grid properties used for the 2-D test cases , and is comparable to grids described in the literature. This mesh contains 72,975 nodes, with 223 nodes on the slat, 399 on the main element, and 210, 313, and 213 on the fore-, mid-, and aft- flap, respectively. A typical convergence history in terms of the density residual, $\partial\rho/\partial t$, and lift coefficient, Cl, for an NSU2D run is shown in Figure 5.2. Approximately 13 Mwords of memory and 60 minutes of Cray Y-MP CPU time is required for the solution.

5.1. Surface Roughness

In examining the usefulness and practicality of computational methods for analysis of true airfoils, the effects of surface roughness of the input geometry are addressed. While many common test cases used by code developers are smooth, some even defined by a continuous function, geometries studied in aircraft analysis are often taken from an existing wing. The surface description of the TSRV wing comes from splashes, which are molded templates taken of the wing, and these splashes were digitally scanned to produce the surface coordinates used in the computations. The data tend to

include surface irregularities and possible error in the splashes and digitization.

Preliminary computations on the TSRV geometry revealed high frequency oscillations near the airfoil surface, particularly noticeable in the surface Cp distribution. The source of the oscillations was determined to be the waviness in the surface geometry description by finding a direct correlation with the surface curvature. The curvature is defined (as in Ref. 26) as:

$$K = \frac{d^2y/dx^2}{\left(1+\left(dy/dx\right)^2\right)^{3/2}} \tag{5-1}$$

This calculation is applied discretely to the surface co-ordinates using central difference approximations:

$$\left(\frac{dy}{dx}\right)_i = \frac{y_{i+1} - y_{i-1}}{x_{i+1} - x_{i-1}} \tag{5-2}$$

and:

$$\left(\frac{d^2y}{dx^2}\right)_i = \frac{\left(\frac{y_{i+1} - y_i}{x_{i+1} - x_i}\right) - \left(\frac{y_i - y_{i-1}}{x_i - x_{i-1}}\right)}{\frac{1}{2}\left(x_{i+1} - x_{i-1}\right)} \tag{5-3}$$

Plotting surface curvature, K, along with surface Cp values reveals the correlation (Fig. 5.3).

This noise in the solution not only degrades the neatness of the plots, but leads to questions regarding the impact on the turbulence model and artificial viscosity, both of which may be influenced by curvature-induced velocity gradients at the surface. Therefore, the airfoil geometry was smoothed manually by applying a simple spline smoother in a piecewise manner around portions of each element. The new geometry was then gridded and computations were performed. The smoothed geometry is visually identical to the original, but has greatly reduced waviness and the resulting Cp distribution is much smoother, as shown in Figure 5.4. Since the Cp of the smoothed

geometry is essentially the mean of the unsmoothed case, the surface roughness appears to cause no adverse effects, such as additional flow separation. However, because the Cp plots are cleaner, the smoothed geometry is used throughout this study.

5.2. Cove Shape

One advantage of Navier-Stokes solvers is the ability to capture flow phenomena around complex shapes including sharp corners and concave cut-outs such as those created when flaps are deployed. Various alternative solution methods require (or are recommended to be run using) streamlined surfaces to be used rather than cove cut-outs in order for the solution to converge efficiently. One such code is MSES, developed by Mark Drela, which is based on a streamline-based formulation of the Euler equations and an integral boundary layer model[27]. Potential flow codes also often require similar modifications to the surface geometry in high-lift configurations. Although the difference appears minor, the influence of cove flows on the flow through gaps between elements is gaining attention in the literature. Cove fairings which deploy with the flaps to reduce the flow separation in the cove regions may appear on future aircraft.

A comparison is made between the true cove shapes for the TSRV in approach configuration and the streamlined coves used with MSES in a previous study[23]. The two geometries and the surface Cp distributions are shown in Figure 5.5. The primary effect of the cove fairings is a slightly decreased loading on the slat and main element and an increased loading on the flap elements due to the altered cove flows. The change in the location of the main-element leading-edge pressure peaks is due to the removal of the "lip" on the lower surface of the slat in the streamlined case. The flow structure in the vicinity of the main element cove is shown for the two cases in Figure 5.6.

The streamlined cove fairings increase the extent of lower surface attached flow and reduce the circulation on that element, thus diminishing the slat effect on trailing elements. Therefore, with less damping due to inviscid interaction, the trailing element loading increases. In addition, the cove fairings reduce the wake thickness slightly, causing a reduction of viscous damping on the trailing elements. As shown in Figure 5.7, the main-element wake is thinner for the streamlined-cove geometry. As a result of the increased fore-flap loading, the pressure-recovery demands increase and the onset of separation moves forward, from $\eta = 0.924$ with cut-out coves to $\eta = 0.913$ with cove fairings. The increased region of flow separation is indicated by the flattening of surface pressure at the fore flap trailing edge (Fig. 5.5), and causes a thicker wake at the $\eta = 0.950$ station, as shown in Figure 5.7. This trend of increased separation is a result of this specific case, but generally, if the contour chosen for cove fairings approximates the shape of a streamline of the true flow, the impact on the computations is small, on the order of other errors evident in the solution.

5.3. Sweep Theory

The correlation between 2-D computations and flight test data depends highly on the applied sweep correction. Figure 5.8 shows computations using simple sweep theory, the local sweep correction, and local sweep plus the empirical n-factor correction. Experimental data is also shown to reveal errors and the MSES computation from Reference 23 (performed using simple sweep) is included to illustrate the improvement gained by Navier-Stokes solvers. In each case, the α_n required to match the slat pressure distribution was different. For MSES, $\alpha_n = 1.2°$, while for NSU2D using simple sweep theory, $\alpha_n = 2.0°$, with local sweep theory, $\alpha_n = 3.0°$, and with the n-factor, $\alpha_n = 2.5°$. As expected, the local sweep theory provides closer matching along the main

element upper and lower surface, but the more accurate correction to the flaps reveals additional overprediction of the flap loadings. The n-factor variation reduces the flap overprediction drastically, thus making the best correlation, but perhaps artificially so, since the method is empirical, and without solid theoretical justification.

Several issues remain to be addressed regarding the sweep correction. Simple sweep theory accounts purely for sweep, assuming an infinite, untapered, swept wing. The local sweep method improves the correction by introducing the effects of wing taper. Using either method, the downwash due to the vortex system of the 3-D wing is partially accounted for by the α_n correction. The downwash effectively reduces the angle of attack of the flow past the airfoil section. In addition, spanwise and chordwise variations in downwash exist in true flow, and it is possible that these variations explain the apparent validation of the n-factor correlation. Gap size and chordwise variation in downwash are thought to be the primary sources of the overprediction of flap loadings.

5.4. Grid Refinement

In order to have a smooth variation in cell sizes, initial grids were generated with high aspect ratio, viscous cells only near the airfoil surfaces. Yet, the dissipation of shear layers in the solution was observed to correlate with the expanding grid cell sizes (Fig. 5.9). In order to improve resolution of the flow, two types of grid refinement were used. First, an automated solution-dependent refinement was carried out using Meshad of the NSU2D package. A velocity gradient three times the average gradient was the refinement criterion used in an effort to improve resolution of viscous gradients. One region which is notably resolved in this manner is the shear layer in the cove regions, as shown in Figure 5.10. The second method of grid refinement was a whole new

generation of grids using Gridpts and UMESH2D. Specifically, longer wake regions with more nodes in both a streamwise and tangential direction were preserved from the initial hyperbolic grids around the elements. The additional streamwise nodes promote the smooth topology that was previously obtained by shortening the extent of high aspect ratio cells. A portion of the wake grid in the vicinity of the flap elements is shown in Figure 5.11. The sizes of the three meshes tested are listed in Table 5.1.

	Baseline Mesh	Meshad case	Wake case
Total Nodes	72,975	118,157	88,799
Slat Surface	229	327	214
Main Element Surface	399	604	399
Fore Flap Surface	210	307	210
Mid Flap Surface	363	454	319
Aft Flap Surface	213	300	214

Table 5.1 - Mesh sizes for five-element grid comparisons.

The surface Cp distributions and various velocity profiles for solutions on the "baseline", "Meshad", and "wake" grids are shown in Figures 5.12 and 5.13, respectively. Clearly, the Meshad case is limited by the grid topology of the baseline case. If the initial grid is much more coarse than needed, several levels of adaptive refinement are necessary since with each level only one node is added between existing nodes in the regions of high gradients. Perhaps an improved scheme would include logic to add a number of new nodes between two existing nodes based on the size of the local gradient. The results for the wake grids show much better resolution of viscous layers, particularly apparent in the velocity profiles. Mach contours in the slat wake region are shown in

Figure 5.14. Clearly, the lack of resolution in the baseline case (Fig. 5.9) provides very little gradient to cause mesh refinement, so the Meshad case does not resolve the slat wake flow. The wake mesh, however, includes numerous cells in the wake region, particularly with fine spacing in the direction normal to the wake centerline, allowing excellent resolution of the shear layer. The slat wake provides a viscous damping effect on the main element, and this reduced loading on the main element reduces the upwash on the slat, due to the circulation effect as described by A.M.O. Smith. Similarly, the improved resolution of the main- and flap-element wakes increases the extent of the wake deficit region, causing increased damping on the flaps, which decreases the loading.

In a rigorous analysis of the wake-mesh result, one might note that the overall decrease in circulation does decrease the slat loading, so by definition, α_n must be increased to match the slat upper surface pressure of the experiment. For this reason, the wake-mesh case was computed with α_n increased from 3.0° to 3.3°. The effect on the pressure distribution was to raise the slat- and main-element pressure levels to match those found using the other meshes. Yet, the decrease on the flaps remains, since the loading of flap elements are not sensitive to small changes in angle of attack. Therefore, the wake meshes are still advantageous for resolving viscous-flow phenomena and providing a closer correlation with flight.

One obvious problem with wake grids is that the high-aspect-ratio wake cells are concentrated where the panel solution of Gridpts determined the wakes to exist. The advantage of an existing grid is reduced at angles of attack for which the wakes are not aligned where the grid is well resolved, though the larger number of nodes throughout the viscous region does benefit the solution. Generation of additional grids for use at the other angles of attack would be

time consuming since the wake locations are determined at such an early stage in the Gridpts grid generation scheme. Perhaps future grid generators could place a fan of high aspect ratio cells in the critical regions of the flow, making the grid more versatile.

5.5. Transition Specification

In complex multi-element flows, laminar regions along the leading edges of the elements help to reduce the boundary layer momentum thickness, delaying separation and reducing drag while increasing maximum lift. Relaminarization of turbulent attachment-line flows has also been observed in tests[1,3,28]. In order for the computations to best predict the flow, transition should be modeled. The Spalart-Allmaras turbulence model, like many others, allows the specification of laminar regions of the flow along airfoil surfaces. In these laminar regions the source term for the eddy viscosity is turned off.

To assess the effect of specifying transition, the approach configuration was analyzed with laminar flow on the slat from the upper surface trailing edge to the edge of the lip on the lower surface. Figure 5.15 shows the comparison between the fully turbulent result and that with the laminar slat. Although not very evident in the Cp distribution, Table 5.2 shows a 5% decrease in drag, as well as a 0.7% increase in lift due to the laminar flow on the slat, resulting in a 6% increase in the critical aerodynamic parameter L/D. The velocity profiles in Figure 5.16 show the thinner laminar boundary layer on the slat surface which decreases the form drag on that element. The laminar velocity profiles also have a lower velocity gradient in the immediate vicinity of the slat surface than the turbulent case, thus producing less skin friction drag than the fully turbulent flow. The thinner slat wake in the laminar case causes less damping of the main element pressure, resulting in the slight increase in total lift.

	Cl	Cd	L/D
Fully Turbulent	3.509	0.04878	72.05
Laminar Slat	3.534	0.04628	76.36

Table 5.2 - Force coefficients obtained from the surface pressure integration.

5.6. Comparison With Flight Data

The preceding sections illustrate several issues faced in the computational prediction of viscous flow, using 2-D analysis tools and comparing with true 3-D flow. This section shows the best correlation and examines the abilities and limitations of the current methods.

5.6.1. Landing Configuration

The 40° flap setting used during landing provides the primary geometry used in this analysis. The specific case compared here is for a flight angle of attack of 8.12°, M_∞ = 0.24, and Re_∞ = 14.67 million. The best correlation between 2-D N-S computations and flight data was obtained with extended-wake meshes, using the local sweep correction along with the empirical n-factor variation, run at α_n = 3.0°. As shown in Figure 5.17, the surface pressures are well predicted. The computations indicate the location and level of the second pressure peak at the main element leading edge due to the discontinuity where the slat nests in cruise. Most of the pressure distribution along the main element upper and lower surface is predicted accurately. The pressure distribution along the flap lower surfaces is accurately predicted, and though the flap upper surface pressures are somewhat off, the levels relative to each other are good. Although detailed boundary-layer measurements were not conducted in Phase II flight tests, tuft flow observations indicated flow separation on the fore flap, also characterized by the flattening of the pressure near the fore flap trailing edge. Although the computations do not show the flattening of the

surface pressure distribution as much as experimental data, separation is clearly evident in the computed flow field (Fig. 5.18). The usefulness of CFD methods to aid in the understanding of flow structures is further illustrated in Figure 5.19, which shows total pressure contours over the aft portion of the configuration, indicating the growth and interactions of element wakes.

Currently, CFD methods are best used to indicate qualitative information regarding the flow structure, and quantitative data such as variations due to changing flow conditions. However, accurate predictions of specific performance characteristics, such as lift and drag forces and stall angles are still limited. Yet, the comparisons of normal force coefficient, Cn, shown in Table 5.3 indicate improvements in this area.

	Experiment	Simple sweep	Local sweep, n
Slat	0.2240	0.2218	0.2320
Main	2.2603	2.5053	2.3067
Fore flap	0.3345	0.4025	0.3725
Mid flap	0.3515	0.3696	0.3502
Aft flap	0.0450	0.0493	0.0486
Total	3.2153	3.5484	3.3100

Table 5.3 - Cn values obtained from the surface pressure integration.

Several key sources of error can explain the discrepancies between the computations and the flight test results. The major source of error is believed to be in the geometry, namely in the gaps and deflections. The shapes of each individual element are accurate, matching templates on the actual aircraft, but the gaps, overlaps, and angles which significantly affect the interaction of the elements were measured more crudely to construct the computational model. Furthermore, the geometry used is that measured on the ground, whereas the

flight data obviously comes from the lifting geometry which changes with blowback due to play in the linkages and aeroelastic deformations.

Along with the geometry problems, the computational model is limited by the sweep theory used to correlate the 2-D results to 3-D data. The local sweep theory does attempt to account for sweep and taper, and the n-factor correction may account for other 3-D discrepancies which have been observed experimentally. However, these corrections are relatively simple compared to the complexity and detail of the flow scenarios, and are believed to be of first order accuracy.

Additional error in the computational results may be attributed to known numerical errors. Artificial viscosity which provides stability for the computations dissipates gradients. Any lack of grid resolution causes additional dissipation. Furthermore, turbulence modeling is rapidly changing since current methods are still known to fail in regions of separation. The landing configuration of the TSRV geometry has four regions of separated flow due to the coves and the fore-flap upper surface separation, all contributing to errors in circulation as well as the inviscid interactions between the elements. However, the excellent agreement between the computations and 2-D wind tunnel data shown in Section 3 would suggest that the error in the codes is much less than those due to geometry and 3-D flow effects.

5.6.2. Take-Off Configuration

The 15° flap setting used for take-off was also tested using wake-type grids along with a local sweep correction and n-factor variation. Free-stream conditions for the experimental case used here are characterized by $M_\infty = 0.17$, $Re_\infty = 11.85$ million, and $\alpha = 9.5°$. The surface pressures are shown in Figure 5.20. Again, the correlation is very good, with many of the same explanations for error. In particular, the slat gap used for the computations is the same as

that used in Reference 22, but is larger than the gap specified in a recently-acquired model of the geometry. This case brings up an additional difficulty in the computations. Using the NSU2D package to generate grids which preserve cells to resolve wakes requires the structured mesh regions around each element, which are increasingly difficult to work with and to obtain a satisfactory mesh as the gap between elements decreases.

5.7. Sensitivity to Changing Flow Conditions

5.7.1. Angle of Attack Effects

The flow past the approach configuration was computed for a range of angles of attack, and the corresponding pressure distributions are plotted in Figure 5.21. The flight data are presented in Reference 1. The cases of α_n = -2°, 3°, and 8° correlate roughly to flight angles of attack of 2°, 8°, and 13°, respectively. The computations were not matched to specific test points because of the additional CPU time this would consume in the iteration to find the converged solution which best matches the slat pressure distribution. The trends are, nevertheless, clearly illustrated using these test cases. The slat and main element pressure peaks increase drastically and the slat loading moves forward with increased α. At low α, the separated flow in the slat cove suppresses the pressure on the main element leading edge lower surface. At higher angles of attack, the separated flow is better contained in the slat cove region, and the pressure on the main element lower surface is higher. On the flaps, for angles of attack in the range of flight data, the variation in loading due to α is small, in agreement with the test results. The trend is a small decrease in flap loading due to the main element wake thickness growth with increasing α. As in the flight test results, the aft flap pressure distribution is independent of α. The α_n = 13° case represents a higher loading than obtained in flight. The main element upper surface develops a thick boundary layer and the

consequently thick wake drastically suppresses the flap loadings. At the higher loading, the tendency for upper surface separation increases and inaccuracies due to the turbulence model become prevalent.

5.7.2. Reynolds Number Effects

The sensitivity of the approach configuration was also assessed for changes in free-stream Reynolds number. The results are shown in Figure 5.22. In the range of flight conditions, roughly from Re_n = 10- to 16-million (corresponding approximately to Re_∞ = 12- to 20-million), the effect of changing Re_n is very subtle. Boundary layer and wake thickness change very little in this flow regime. On the contrary, the results for Re_n = 1.5 million show a significant effect. This case was chosen to approximate a typical wind-tunnel model at standard atmospheric conditions. The change in the pressure distribution illustrates the problem of extrapolation from wind-tunnel results to predict flight performance. At low Re_n, viscous effects have a more significant effect due to the thicker boundary layers and wakes, which suppress the loading of trailing elements. Also, in experiments at different Re_n, the mechanisms of transition and separation act differently.

5.8. Gurney Flaps

The concept of the Gurney flap which originated in racing car spoiler design has found practical application on aircraft wings[29]. This small flat plate placed at the trailing edge of an airfoil, normal to the lower surface, effectively shifts the location of the Kutta condition, increasing the circulation and hence the lift of the element. The increase in lift comes primarily from the effective increased camber on the lower surface without adversely disturbing the upper surface flow. The profile drag of the airfoil generally increases with the addition of the Gurney flap, but often the percentage increase in lift is greater, resulting in an increased lift-to-drag ratio and therefore better efficiency and

performance. Because of the simple geometry of the Gurney flap, construction is simple and weight is low, and deployment with the flap system is easily accomplished. Various theories and experiments describe a flow structure downstream of a Gurney flap which has dual recirculation regions[29,30].

Gurney flaps of length 0.01c and 0.02c were added to the aft flap in the computational geometry. In order to later compare with the results of the upcoming Phase III flight tests, the devices were modeled as "L"-shaped brackets, including the base required for mounting to the wing lower surface. The flow structure in the vicinity of the Gurney flap is shown in Figure 5.23. The dual recirculation regions downstream of the flap are predicted as described in the literature. No grid refinement was necessary to reveal this phenomenon. Some separation exists in the region upstream of the Gurney flap, but the primary flow turns smoothly downward with the added camber of the lower surface. The Mach contours downstream of the Gurney flap show the shrinking of the recirculating wake as the flow moves away from the airfoil (Fig. 5.24). The impact of the Gurney flaps on the loading of the system is shown in Figure 5.25. The circulation of the entire system increases with the addition of the trailing-edge device, illustrating the elliptic behavior of the flow and the increased circulation of the airfoil system. Along with the increase in lift, the Gurney flaps produce a substantial drag rise, primarily in the form of pressure drag, as might be expected from the orientation of the Gurney flaps in the 40° flap setting. The corresponding lift-to-drag ratio is decreased, as shown in Table 5.4. Yet, in the approach configuration, drag can be a favorable quality, assisting the deceleration of the aircraft, and high lift is often more important than high L/D.

	Cl	Cd	L/D
Baseline Airfoil	3.509	0.04878	72.05
1% Gurney Flap	3.655	0.05245	69.69
2% Gurney Flap	3.710	0.05566	66.65

Table 5.4 - Force coefficients integrated from the surface pressure distributions for the approach configuration (40° flaps).

The effects of 1% and 2% Gurney flaps on the take-off configuration are shown in Figure 5.26. Again, the primary effect of the flaps is an increased circulation on the entire system. The corresponding force coefficients are listed in Table 5.5.

	Cl	Cd	L/D
Baseline Airfoil	2.208	0.03615	61.10
1% Gurney Flap	2.299	0.05419	42.43
2% Gurney Flap	2.388	0.06175	38.67

Table 5.5 - Force coefficients integrated from the surface pressure distributions for the take-off configuration (15° flaps).

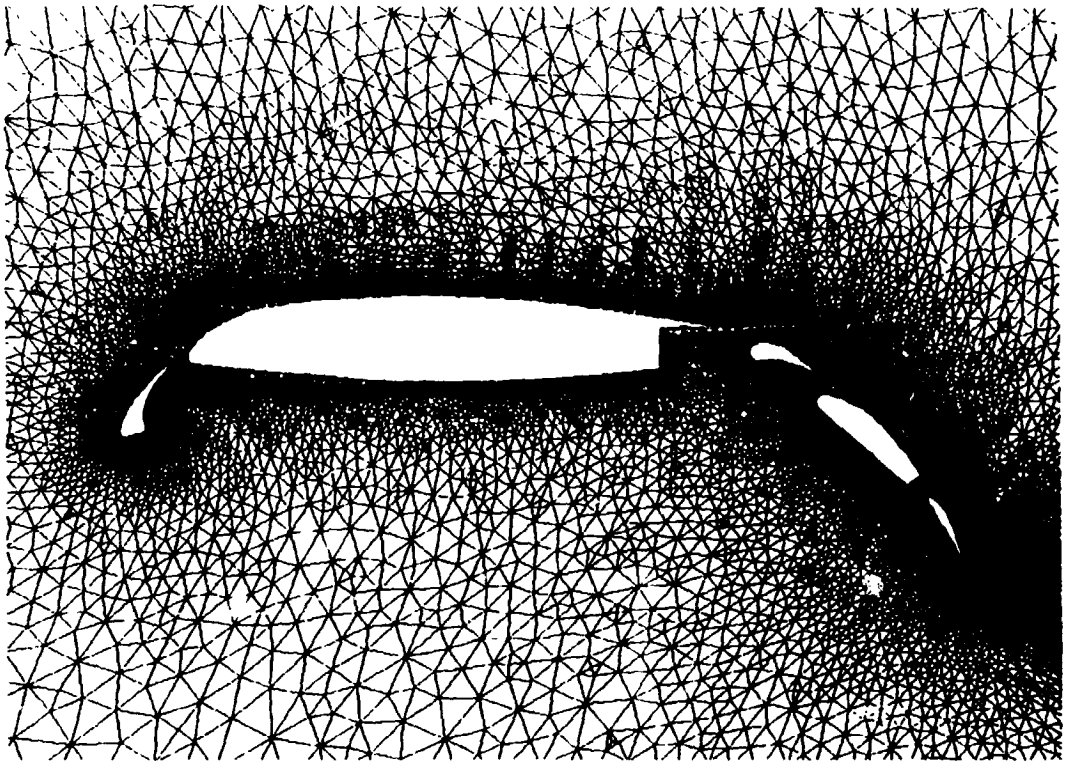

Figure 5.1 – Typical grid for five-element airfoil computations.

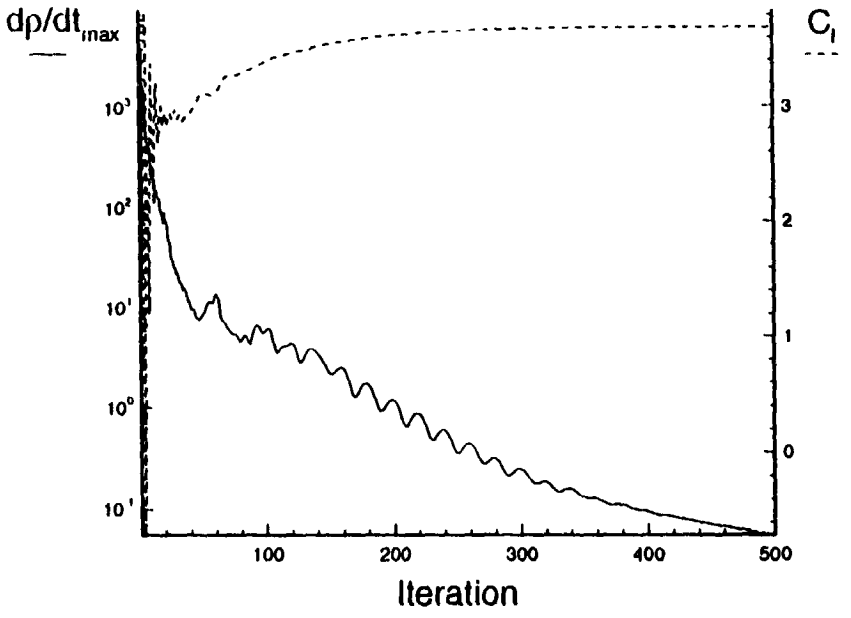

Figure 5.2 – Typical convergence history for an NSU2D solution.

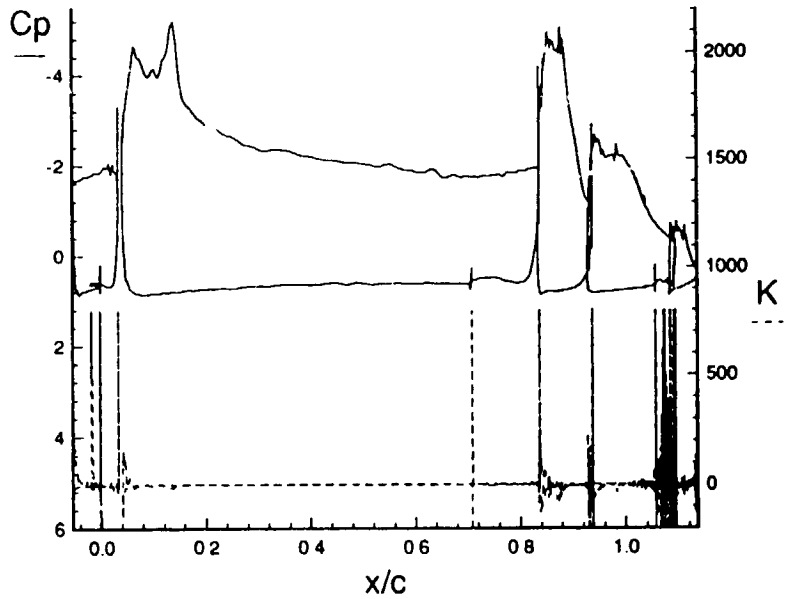

Figure 5.3 - Correlation between waviness in surface pressure computations and airfoil surface curvature, K.

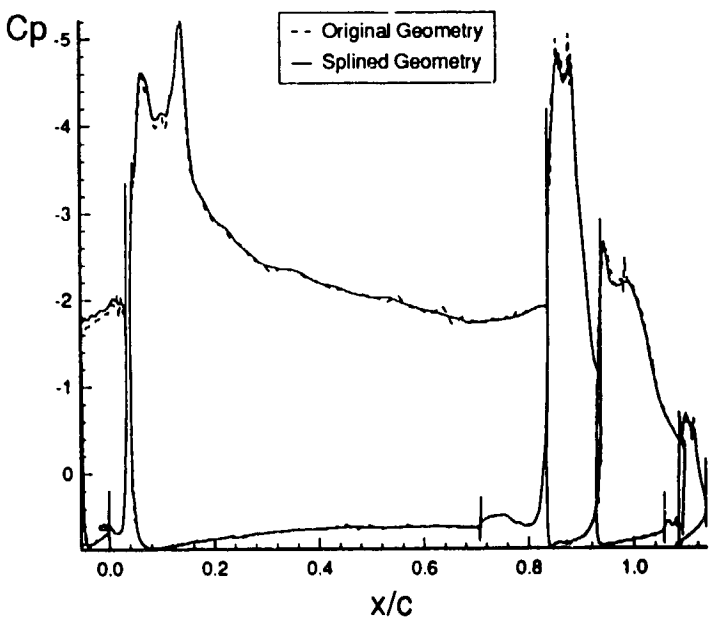

Figure 5.4 - Effect of smoothing airfoil surface coordinates on computed surface pressure distribution.

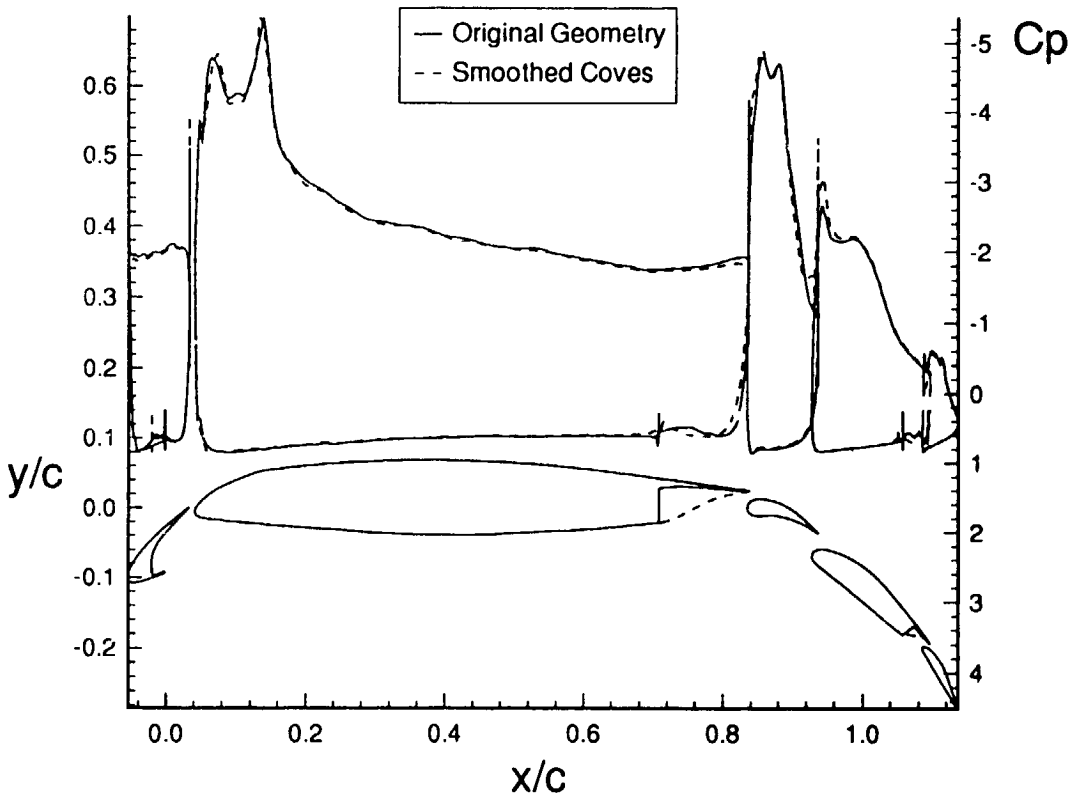

Figure 5.5 - Effect of cove shape modeling on surface pressure.

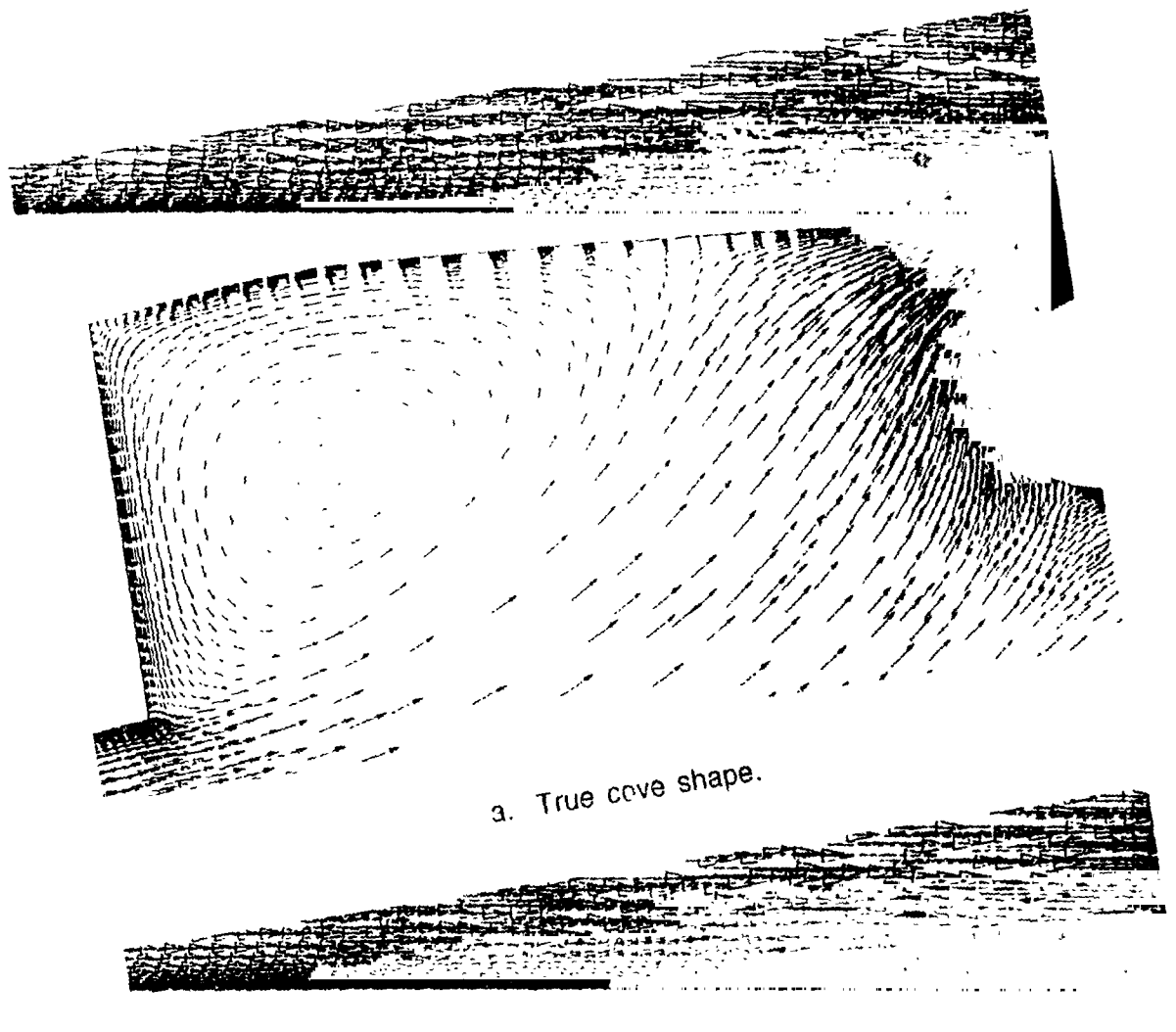

a. True cove shape.

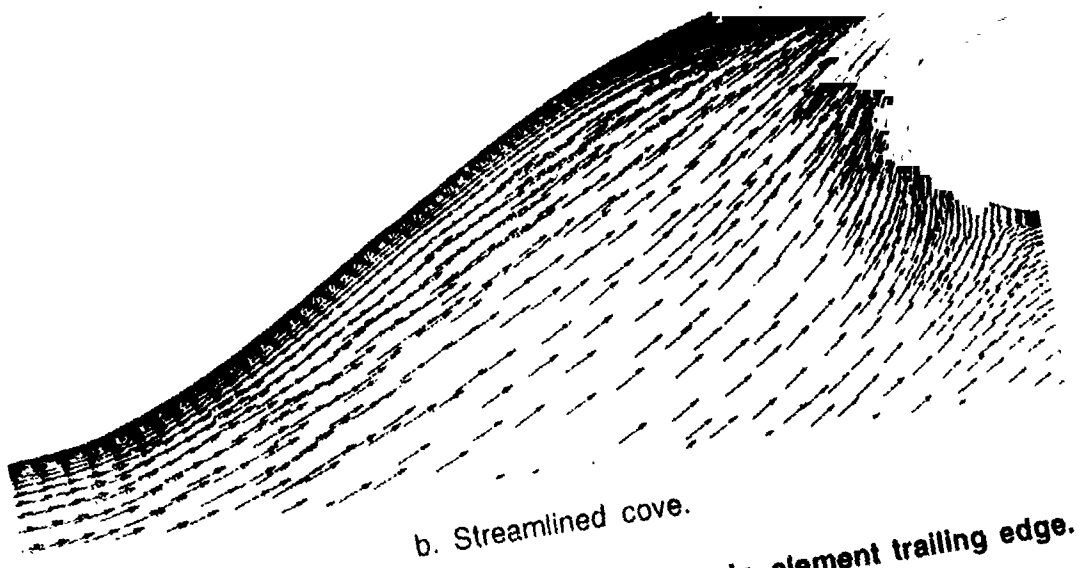

b. Streamlined cove.

Figure 5.6 – Flow structure in vicinity of main-element trailing edge.

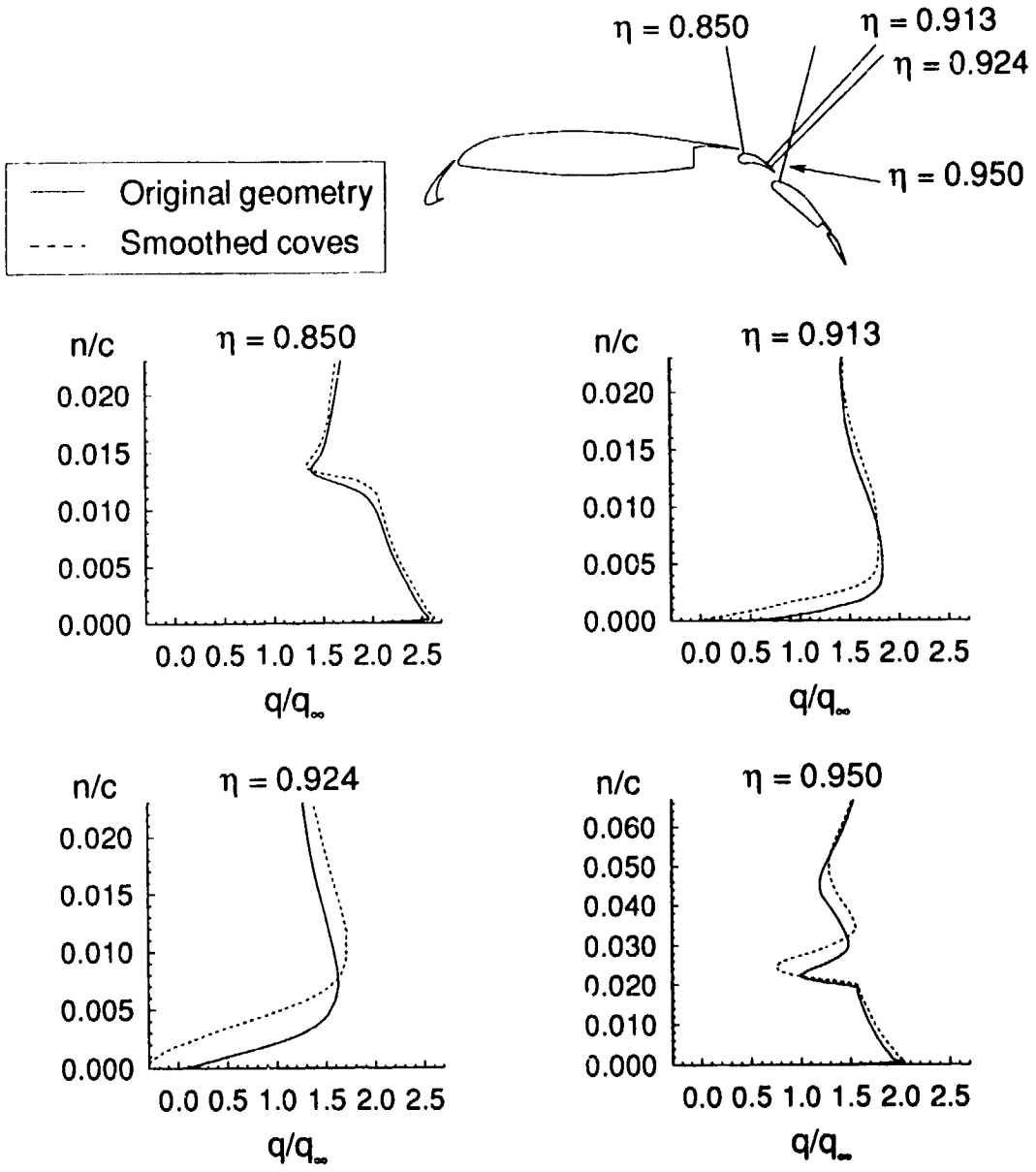

Figure 5.7 - Effect of cove shape modeling on boundary-layer velocity profiles.

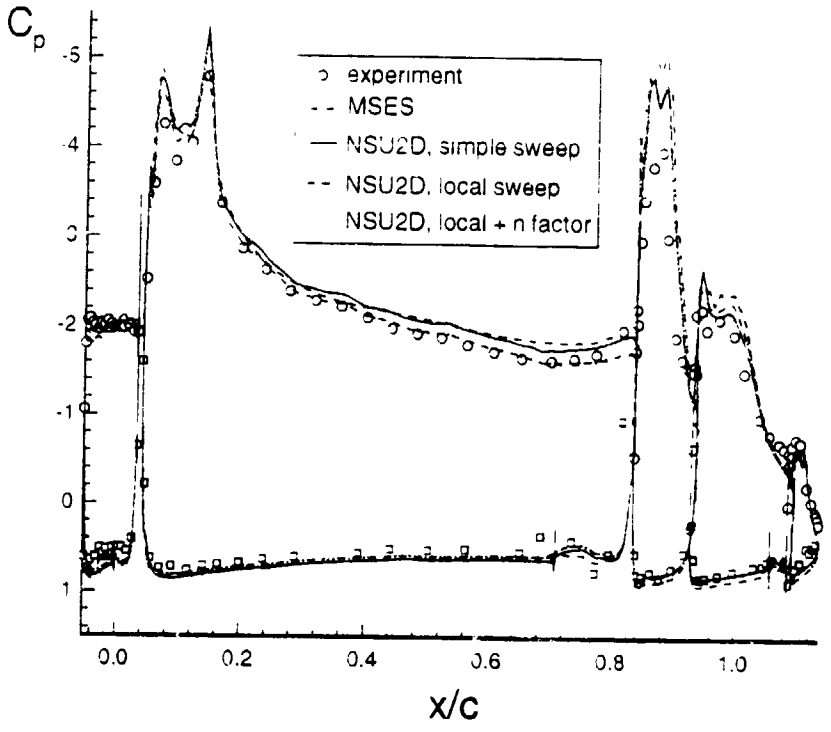

Figure 5.8 - Effect of sweep theory on surface pressure distribution. (M_∞ = 0.24, Re_∞ = 14.67 million, α = 8.3°)

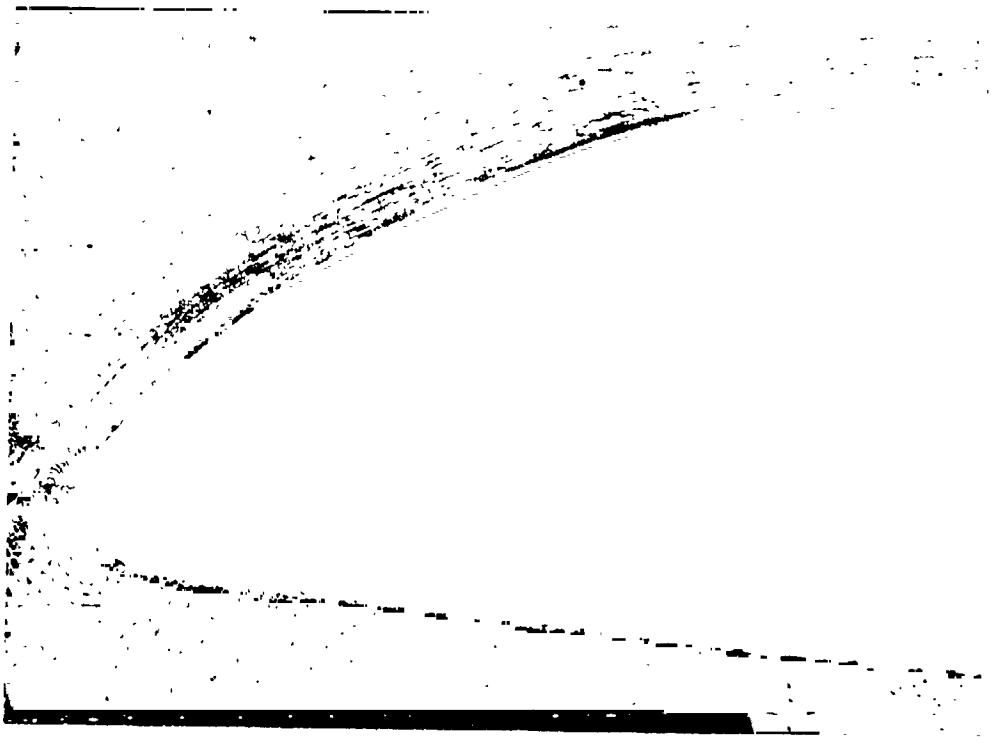

Figure 5.9 – Mach contours overlaid on baseline mesh in vicinity of main-element leading edge showing dissipation of slat wake.

NOTE: This figure was originally in color and the image shown here lacks the clarity provided by the color overlay.

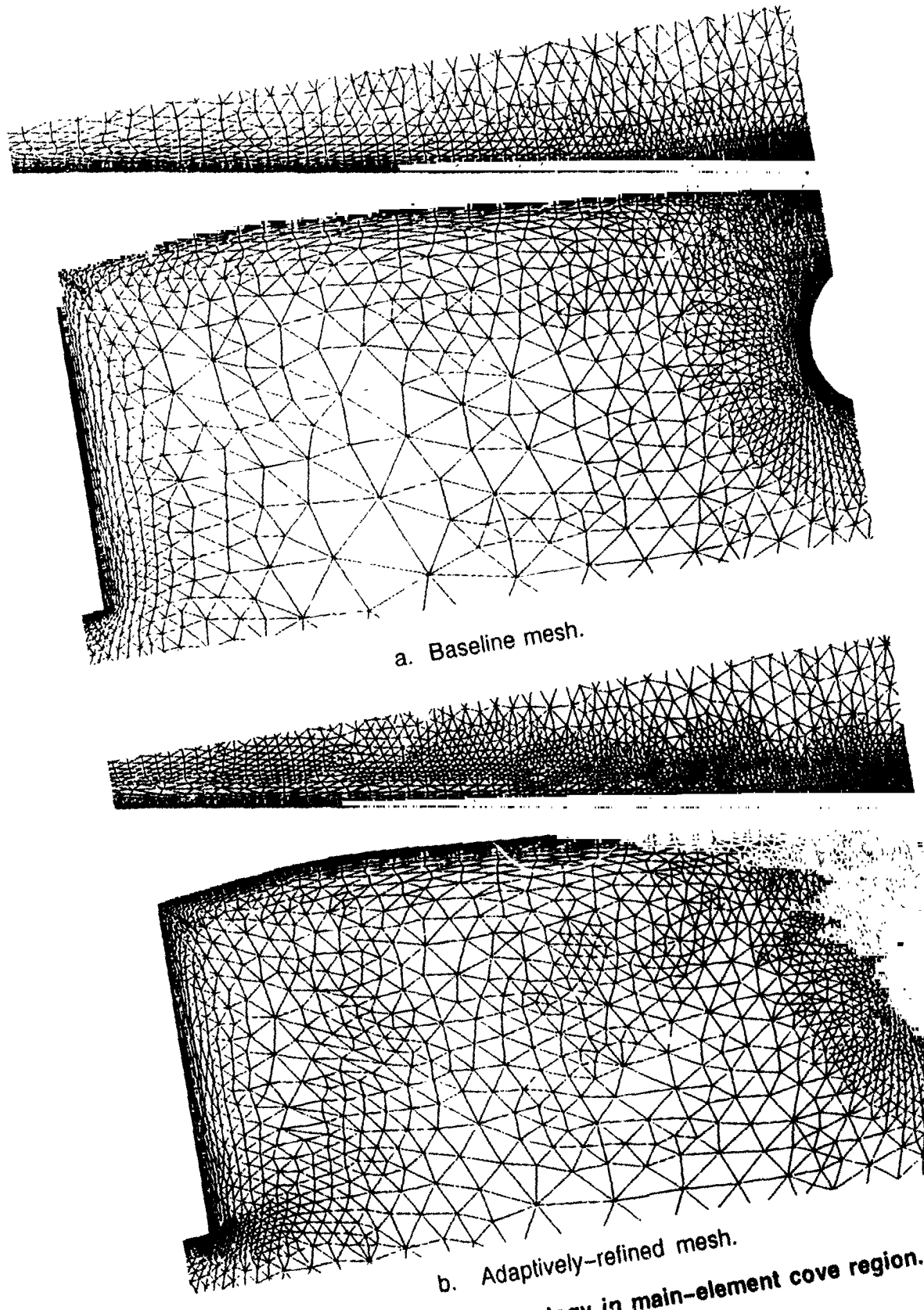

a. Baseline mesh.

b. Adaptively-refined mesh.

Figure 5.10 – Grid topology in main-element cove region.

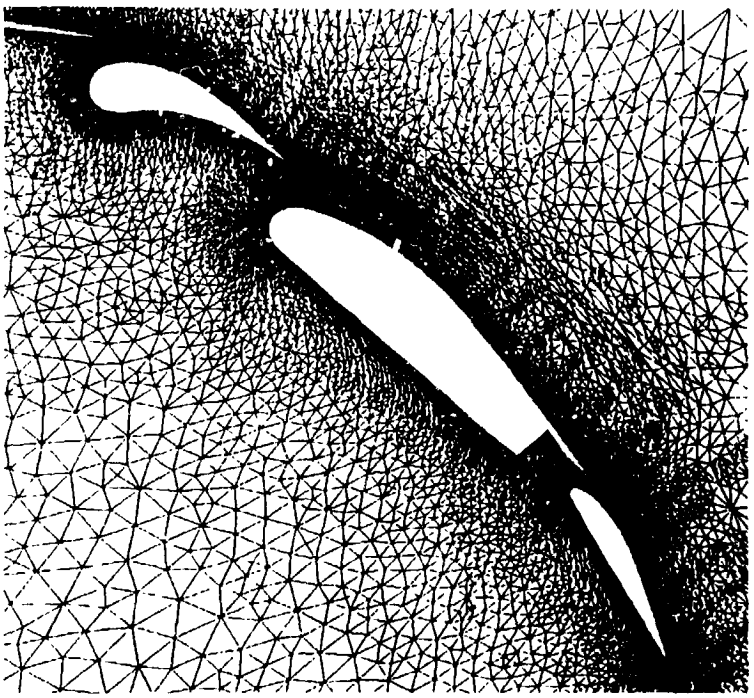

a. Baseline mesh.

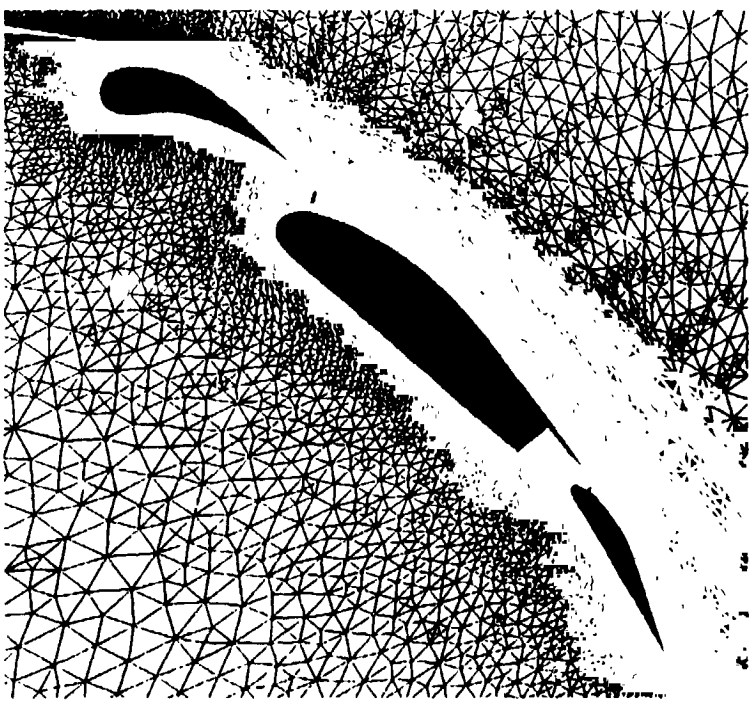

b. Wake mesh.

Figure 5.11 – Grid topology in vicinity of flap elements.

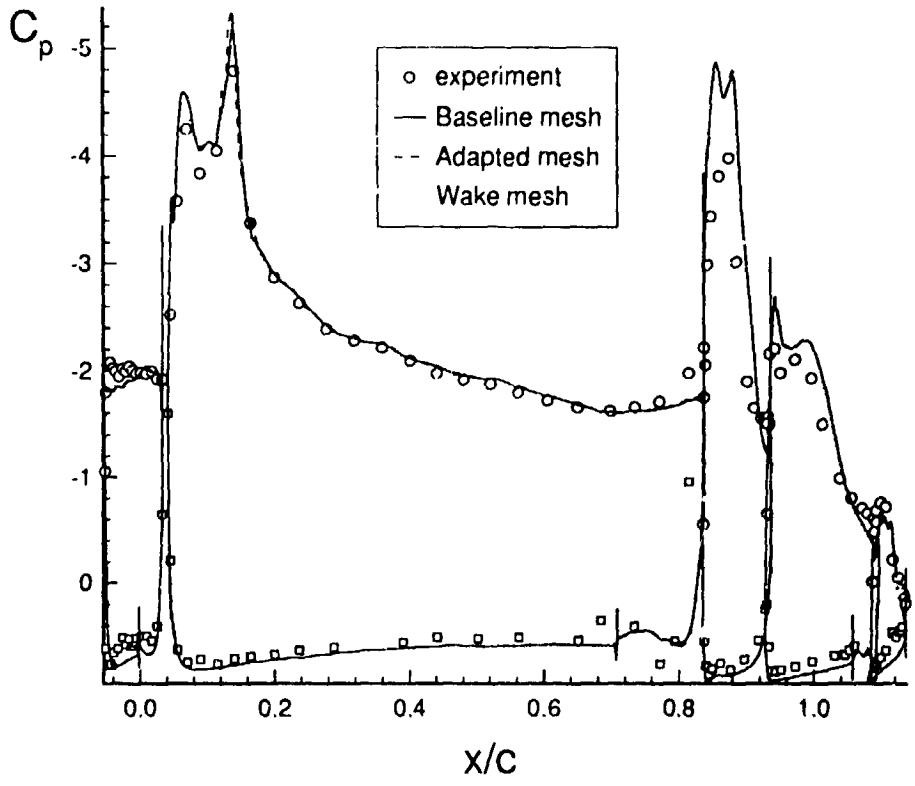

Figure 5.12 - Effect of mesh on computed surface pressure distribution.

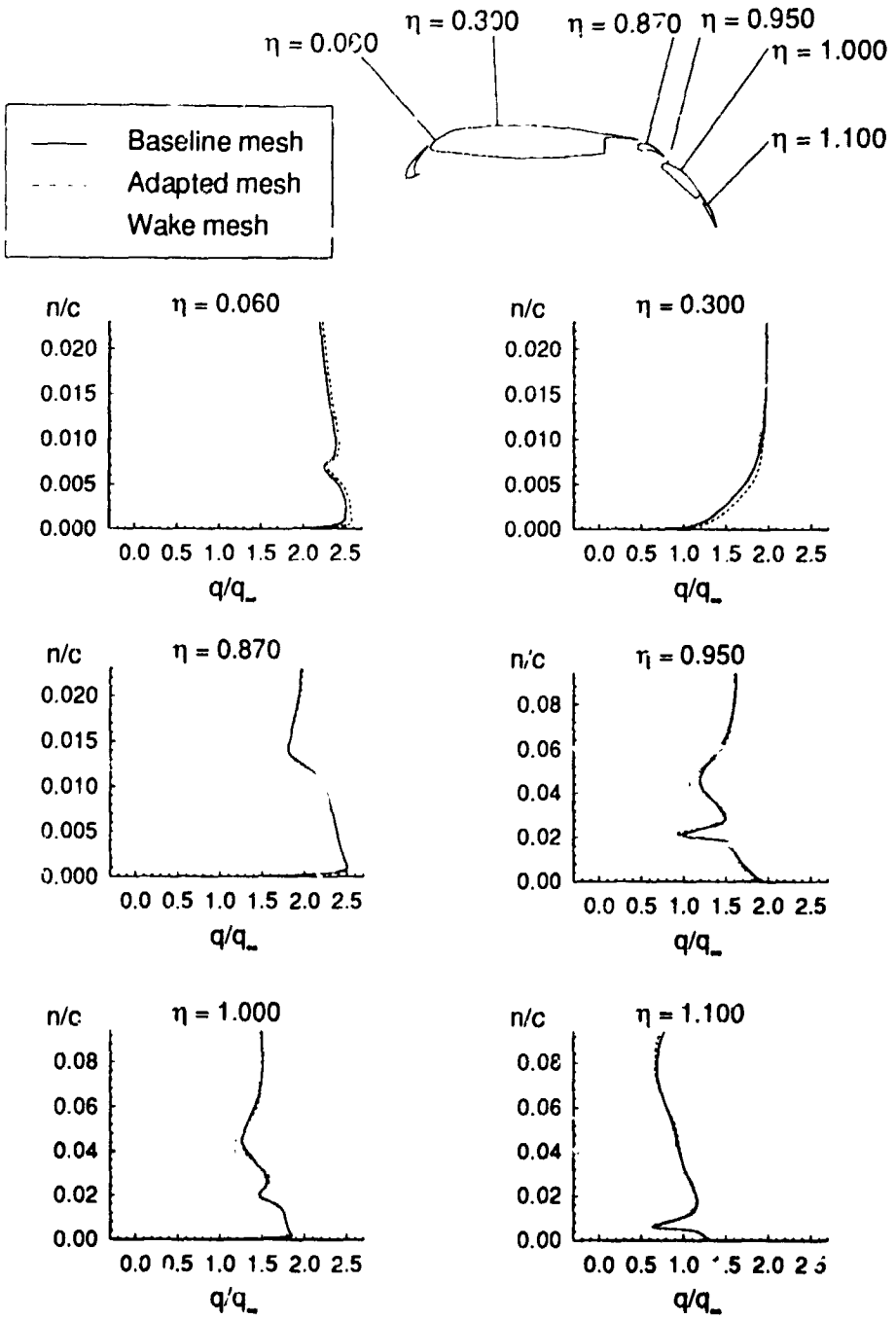

Figure 5.13 - Effect of mesh on boundary-layer velocity profiles.

a. Adaptively–refined mesh.

b. Wake mesh.

Figure 5.14 – Mach contours overlaid on computational mesh in vicinity of main–element leading edge showing resolution of slat wake.

NOTE: This figure was originally in color and the image shown here lacks the clarity provided by the color overlay.

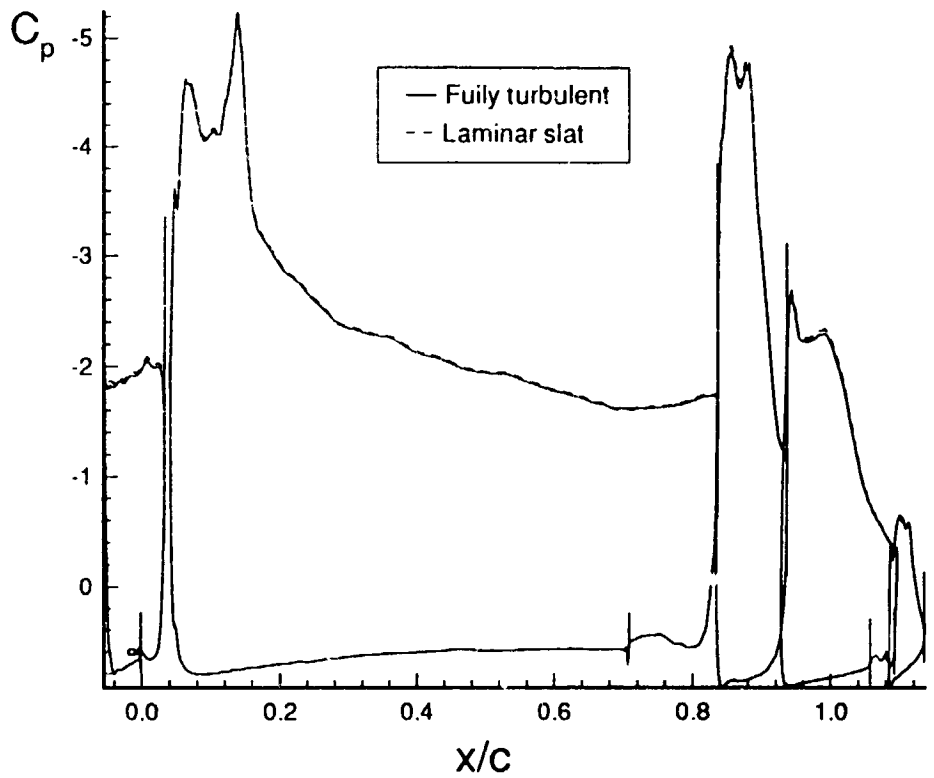

Figure 5.15 - Effect of laminar slat flow on surface pressure distribution.

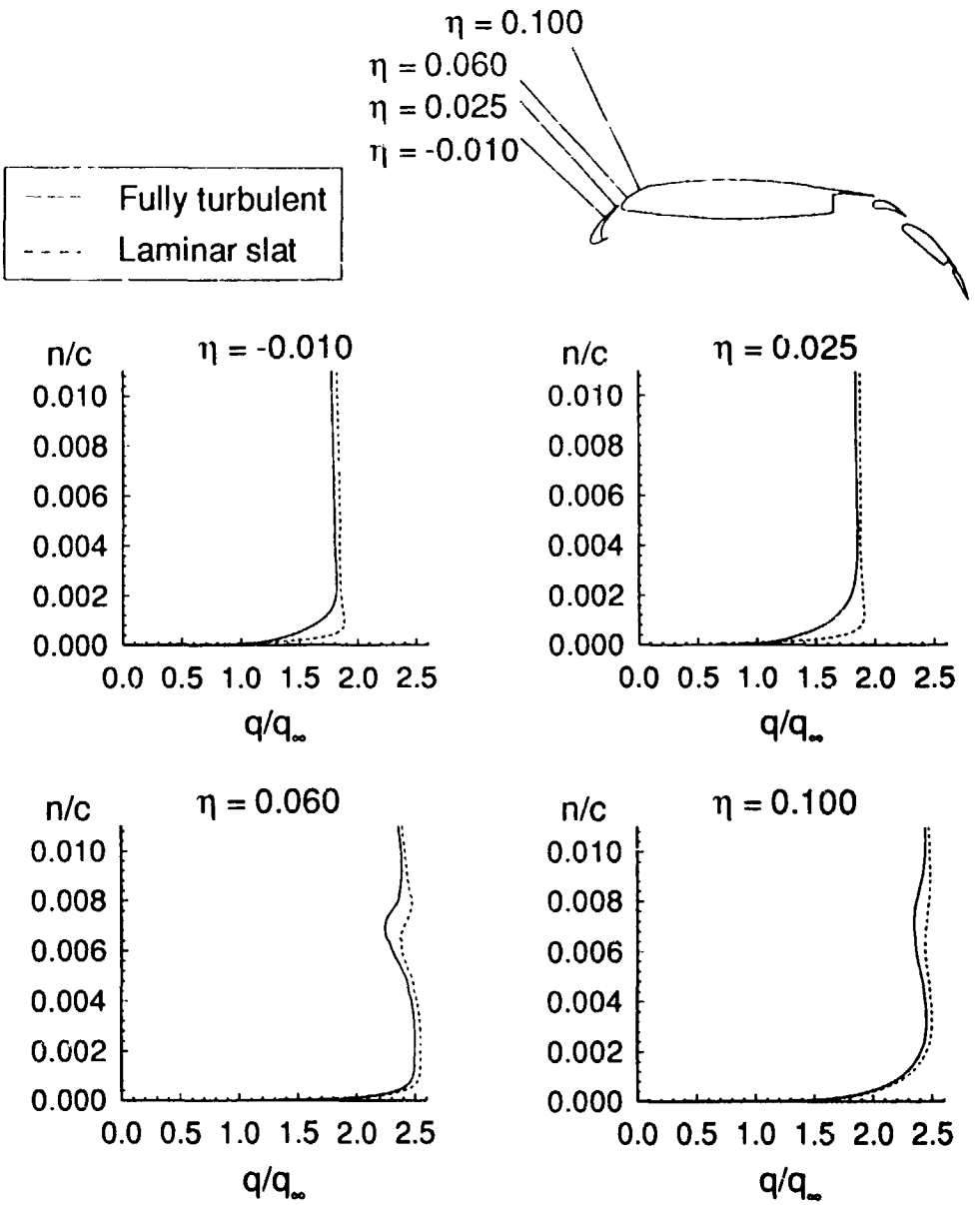

Figure 5.16 - Effect of laminar slat flow on boundary-layer velocity profiles.

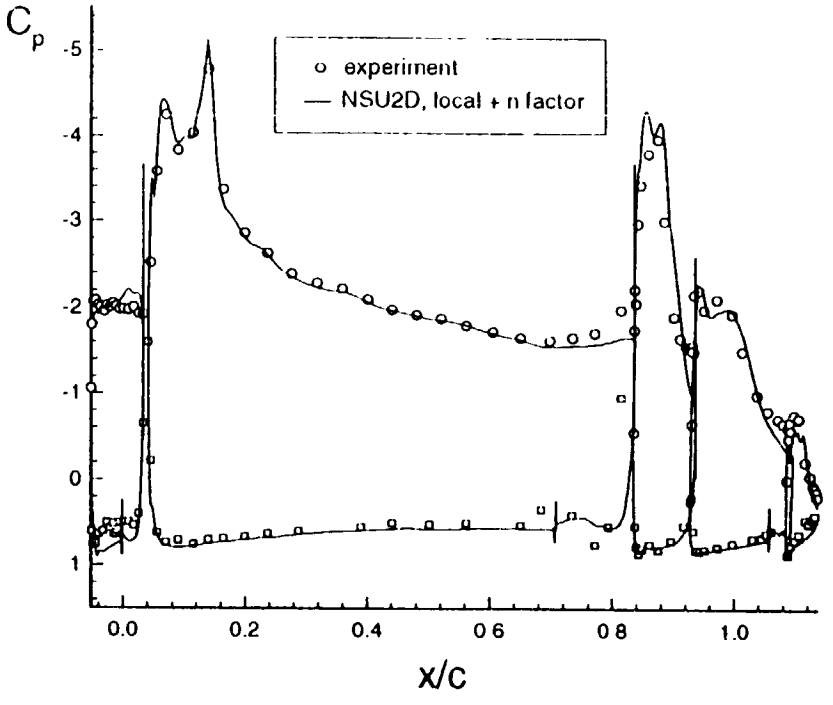

Figure 5.17 - Best correlation with flight results for approach configuration (40° flaps), using wake meshes, local sweep correction + n-factor. (M_∞ = 0.24, Re_∞ = 14.67 million, α = 8.3°)

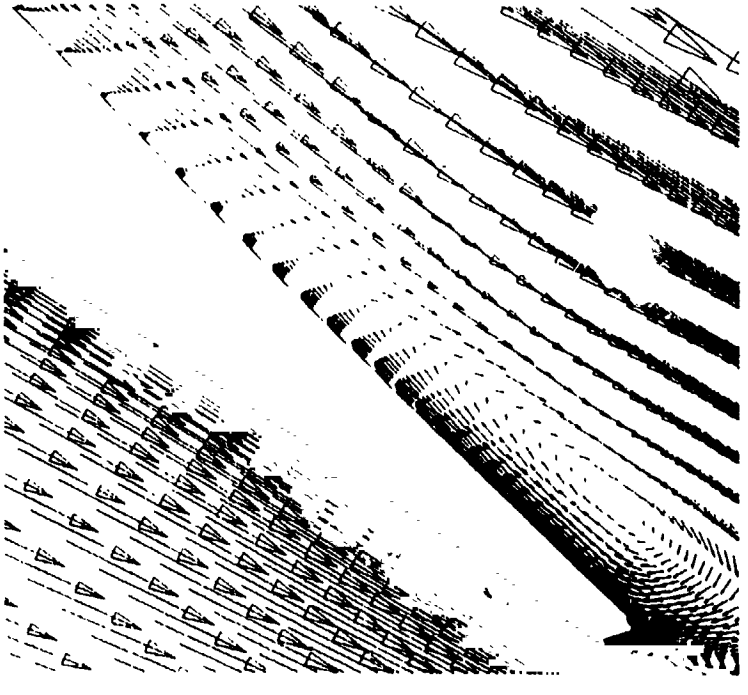

Figure 5.18 – Velocity vectors showing separated-flow region on fore-flap trailing-edge upper surface.

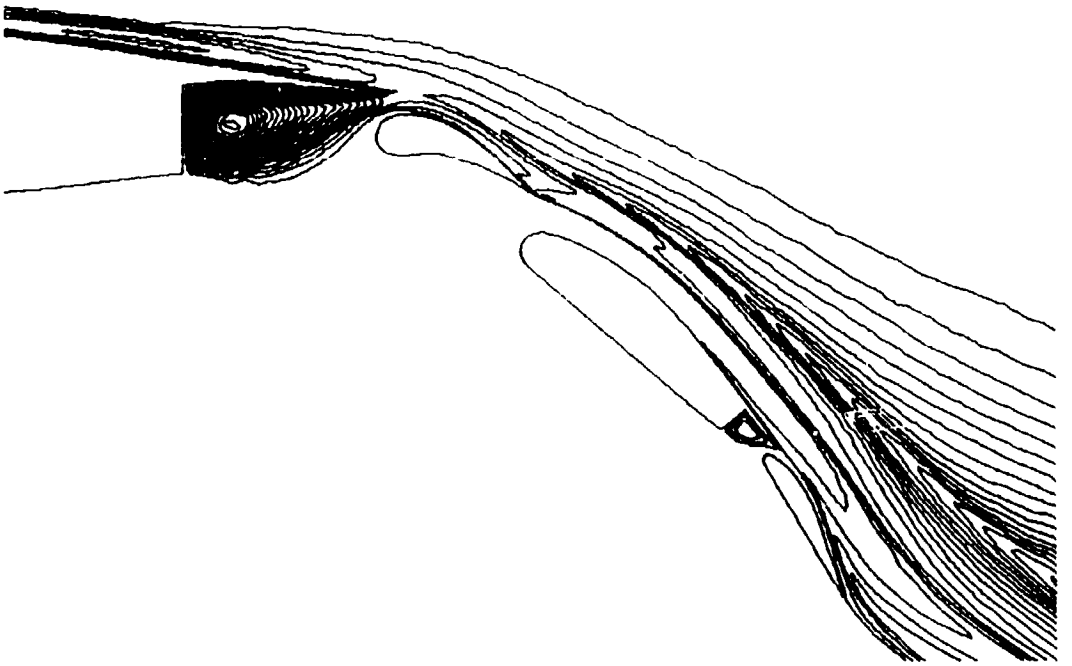

Figure 5.19 – Total pressure contours in vicinity of flap elements.

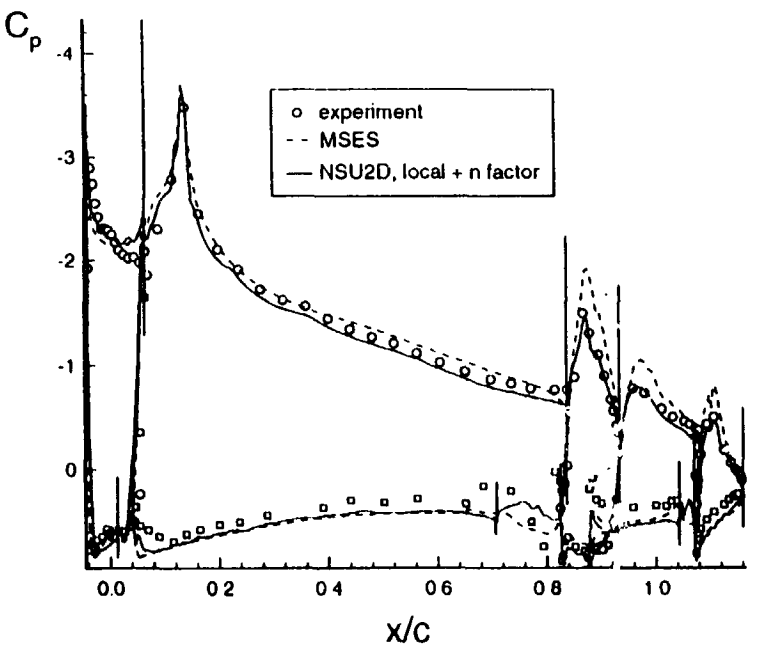

Figure 5.20 - Best correlation with flight results for take-off configuration (15° flaps), using wake meshes, local sweep correction + n-factor. (M_∞ = 0.17, Re_∞ = 11.85 million, α = 9.4°)

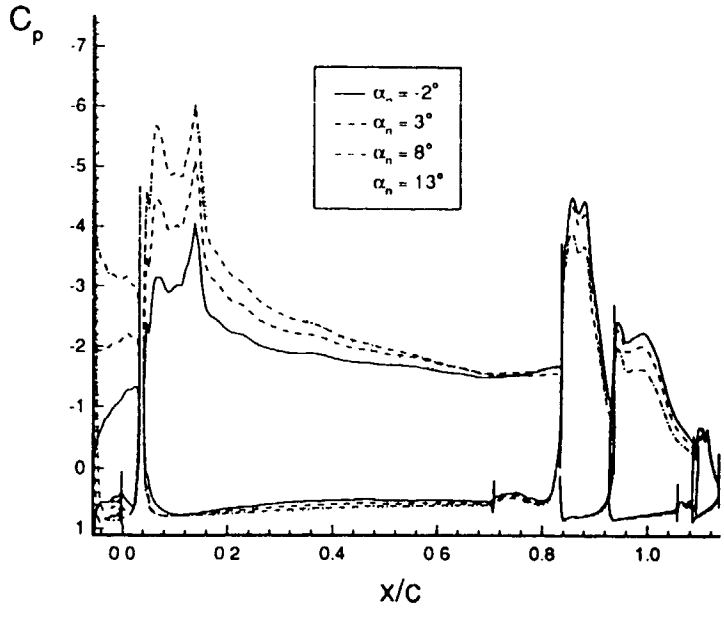

Figure 5.21 - Sensitivity of the pressure distribution to freestream angle of attack.

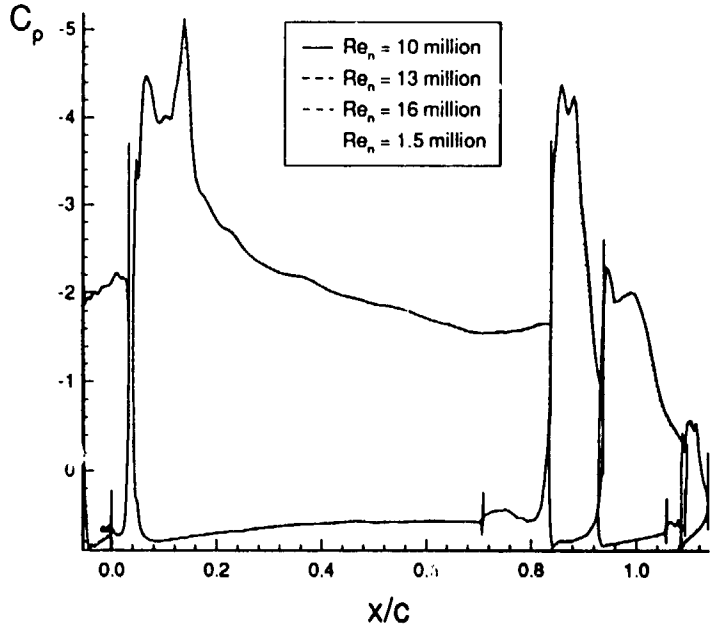

Figure 5.22 - Sensitivity of the pressure distribution to Reynolds number.

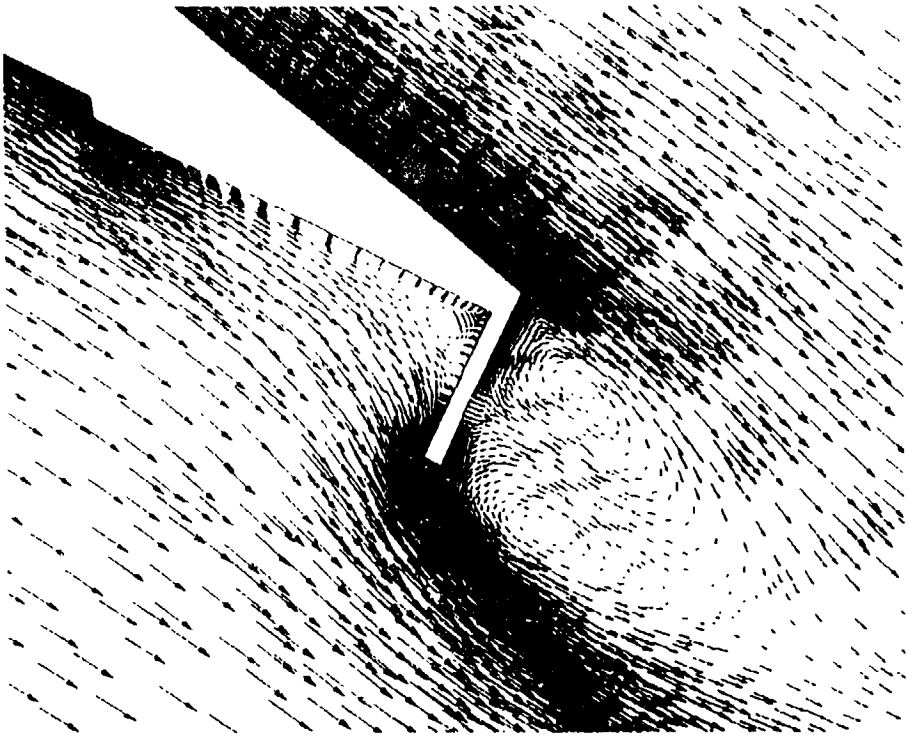

Figure 5.23 – Gurney flap geometry and local flow structure.
(1% flap, 15° flap setting)

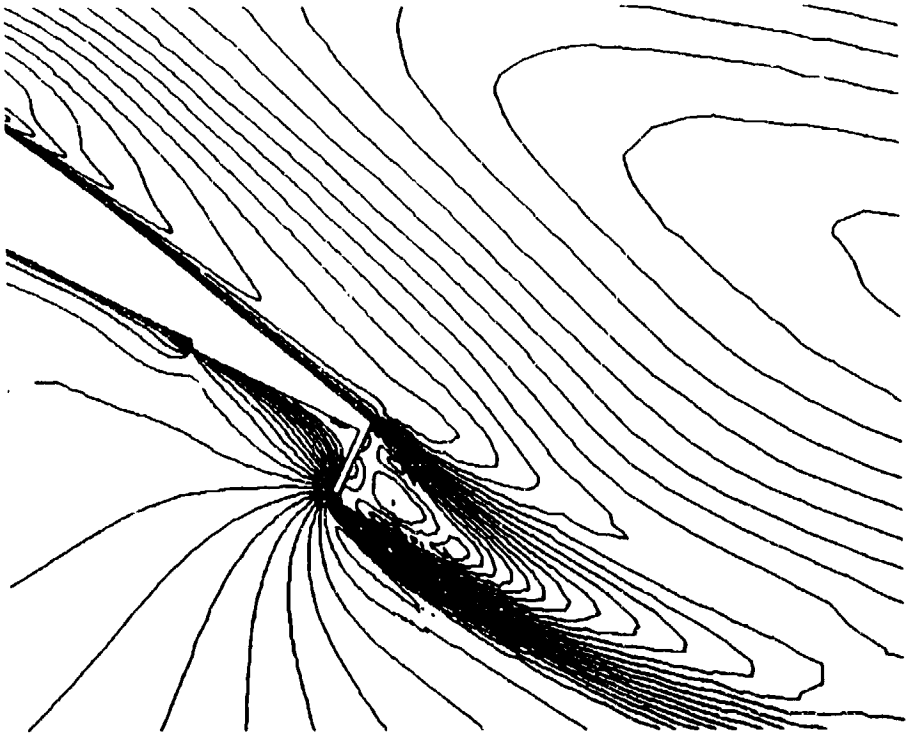

Figure 5.24 – Mach number contours in vicinity of the Gurney flap.

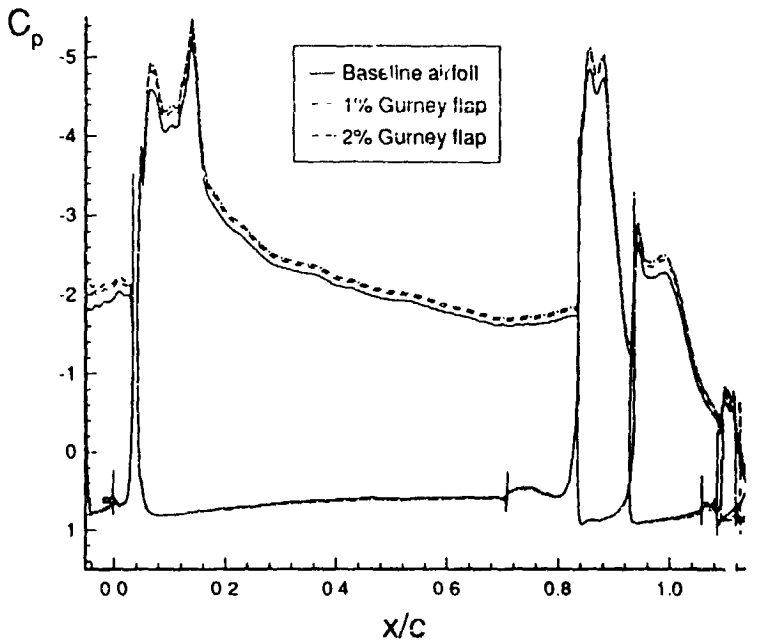

Figure 5.25 - Effect of 1% and 2% Gurney flaps on the surface pressure distribution for approach configuration (40° flaps).

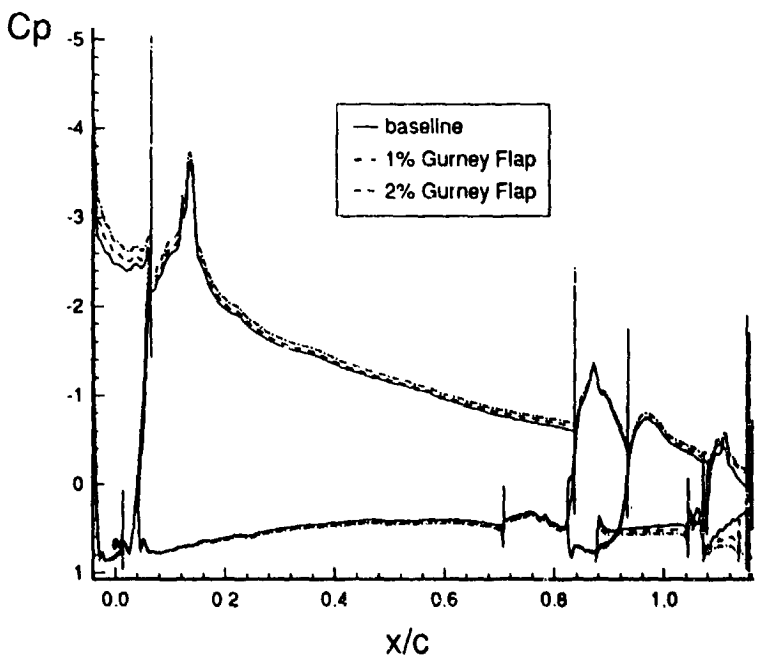

Figure 5.26 - Effect of 1% and 2% Gurney flaps on the surface pressure distribution for take-off configuration (15° flaps).

6. Conclusions

The impact of high-lift performance on the overall performance of a subsonic transport aircraft justifies comprehensive studies of the flow past multi-element airfoil systems. Numerous wind-tunnel- and flight-test programs have provided tremendous insight into the high-lift flow regime, but only with the support of a tremendous budget. In an effort to reduce the expense of analyzing numerous configurations and the effects of changes in freestream conditions and geometry, recently developed Computational Fluid Dynamics (CFD) methods are being applied to multi-element airfoil systems. As part of a multi-phase high-lift flight research program, computational studies are being conducted on the NASA Langley Transport Systems Research Vehicle (TSRV). In this study, the capabilities of two production codes which solve the 2-D Navier-Stokes equations on unstructured grids are assessed. Computational results are compared to wind-tunnel and flight-test data. The effects of surface roughness, cove shape modeling, sweep theory, grid refinement, and transition specification are addressed. In addition, the trends associated with changing freestream angle of attack and Reynolds number are shown. Finally, the aerodynamic effects of Gurney flaps are predicted. Several primary conclusions resulting from this study are summarized here:

- CFD tools accurately predict the 2-D viscous flow past multi-element wing sections tested in wind tunnels in the absence of massive upper-surface separation.
- Application to 3-D flight-test studies introduces additional complications in terms of geometry inaccuracies and sweep theory to correct 2-D computations for the effects of sweep, taper, and finite wing effects.

- Surface roughness in the airfoil geometry used for computations causes waviness in the surface pressure distribution, but does not c ıstically affect the solution in ter ns of the average levels, or the onset of separation.
- The common practice of modeling coves with smooth fairings for computations causes a small decrease in circulation on the altered elements, and slightly thinner wakes, and therefore a slightly increased loading on trailing elements. However, the overall effect on the flow is small.
- Sweep theory has a first-order influence on the comparison with 3-D flight data. An improvement over simple sweep theory accounts for taper effects by using local sweep angles, which vary along the chord, rather than a nominal angle. An empirical "n-factor" alteration to the sweep correction applied to Cp improves the comparison with flight, but without solid theoretical justification.
- Grid refinement improves resolution of viscous-flow phenomena, such as wakes and confluent boundary layers, but with only a small effect on the surface pressure distribution.
- Generating grids with additional cells in wake regions, and in particular, high aspect-ratio cells with fine spacing normal to streamlines is a more efficient means of resolving viscous flows than using adaptively-refined meshes, which require several levels of refinement and introduce more new nodes.
- Specifying a region of laminar flow using the Spalart-Allmaras turbulence model causes insignificant change to the flow prediction. This result may seem to show a weakness of the model, but it may also be interpreted as an indication that the fully-turbulent solution correctly applies small levels of eddy viscosity in regions where the true flow is laminar.
- Using the local sweep correction, along with the n-factor modification, the N-S computations using wake meshes correlates well with flight-test results,

including the prediction of separated-flow regions. Discrepancies are attributed to sweep theory and inaccuracies in the model geometry.

- MSES provides an excellent prediction of surface pressures using much less memory and CPU time than N-S solvers, but is more limited in terms of geometry and flow conditions, and provides less detail of the flow structure.
- The computed trends of changing angle of attack agree with flight results. Slat and main-element loading increases with increasing α, while flap loading decreases slightly due to the slat effect as well as viscous damping resulting from the thicker wakes. However, due to known inaccuracies in the turbulence modeling, the prediction of maximum lift was not attempted.
- The computations show negligible sensitivity of the TSRV wing section to changes in Reynolds number in the range of flight. A prediction using a low Reynolds number, comparable to that of an atmospheric wind tunnel, shows a significant decrease in circulation and loading.
- The addition of 1% and 2% Gurney flaps to the aft flap produce the expected flow structure, as well as lift increments, but a decrease in L/D for this configuration.

The results of this study illustrate the capability of current computational methods to accurately predict the flow past multi-element airfoil systems. Furthermore, 2-D solvers, which are manageable with current computer resources, can provide an accurate representation of 3-D flow, when used in conjunction with sweep theory. The sweep corrections, applied here in the form of pre- and post-processing operations, attempt to account for the effects of wing sweep, taper, and downwash from the tip vortices. Until 3-D viscous-flow solutions become practical, further improvements to the intermediate step of quasi-3-D solution methods are necessary. A potential improvement would be to add the third dimension to the equations, but still solve the equations on a

2-D grid, with gradients in the direction normal to the 2-D cut turned off. This would eliminate the need for pre- and post-processing operations and would allow the development of a 3-D boundary layer. Another area in need of attention, particularly in the correlation with flight test data, is the modeling of the geometry. Multi-element airfoil flows are highly sensitive to changes in incidence angles and gaps. The geometry measured on the ground may be quite different from that in flight under loading, so the computational model should, if possible, be made from the loaded system. For this reason, upcoming flight tests of the TSRV will include OPTOTRAK instrumentation to measure movement occurring in flight. Despite current limitations and known errors, CFD methods can provide tremendous insight of multi-element high-lift flows.

Appendix 1: Upwinding of Convection Terms

CFD methods require smoothing or diffusion for stability and consequently to converge on a solution. This diffusion is commonly added explicitly into the equations being solved. An alternative method of achieving the same result is upwinding of the convective terms in the discrete formulation. While the upwind method applies to multi-dimensional flows solved using finite-element and finite-volume methods, the analysis of this method is most clearly shown for one dimension using a finite-difference approach. The model equation used here is the simple linear convection equation, known as the wave equation:

$$\frac{\partial u}{\partial t} = -c\frac{\partial u}{\partial x} \tag{A1-1}$$

If artificial viscosity was explicitly applied, the equation solved would take the form,

$$\frac{\partial u}{\partial t} = -c\frac{\partial u}{\partial x} + \alpha\frac{\partial^2 u}{\partial x^2} \tag{A1-2}$$

where α is the coefficient of artificial viscosity, $\alpha << 1$. Note that α must be a function of Δx in order for Eq. (A1-2) to be consistent with Eq. (A1-1) as $\Delta x \rightarrow 0$.

Using upwind differences, the convective terms of Eq. (A1-1) are discretized as:

$$-c\frac{\partial u}{\partial x} \approx \begin{cases} -c\dfrac{u_i^n - u_{i-1}^n}{\Delta x}, & c > 0 \\ -c\dfrac{u_{i+1}^n - u_i^n}{\Delta x}, & c < 0 \end{cases} \tag{A1-3}$$

Applying truncation error analysis to the differenced terms in Eq. (A1-3), we expand the terms that are not at time level, n, and at space index, i, using Taylor series expansions. For the case when c > 0, we have:

$$u_{i-1}^n = u_i^n - \Delta x \left.\frac{\partial u}{\partial x}\right|_i^n + \frac{\Delta x^2}{2}\left.\frac{\partial^2 u}{\partial x^2}\right|_i^n - O(\Delta x^3). \qquad \text{(A1-4)}$$

In a complete truncation error analysis, the discretization of the time-dependent derivative would also be evaluated, using Taylor series expansions of those terms which are not at time level, n. However, the purpose of this discussion is to show the relationship between different discrete forms of the space derivative, so it is assumed that the same time discretization is used in both cases, and an analysis of the discrete time terms is not shown here.

Substituting Eq. (A1-4) into Eq. (A1-3), for c > 0 yields:

$$-c\frac{\partial u}{\partial x} = -c\frac{u_i^n - u_i^n + \Delta x \left.\frac{\partial u}{\partial x}\right|_i^n - \frac{\Delta x^2}{2}\left.\frac{\partial^2 u}{\partial x^2}\right|_i^n + O(\Delta x^3)}{\Delta x} \qquad \text{(A1-5)}$$

which reduces to:

$$-c\left.\frac{\partial u}{\partial x}\right|_i^n + \left(c\frac{\Delta x}{2}\right)\left.\frac{\partial^2 u}{\partial x^2}\right|_i^n + O(\Delta x^2). \qquad \text{(A1-6)}$$

As might be expected from this one-sided difference, the truncation error of the discrete formulation is first order. Ignoring the terms of second order and higher, the numerical error, ε in the upwind difference method shown here is:

$$\varepsilon = \left(c\frac{\Delta x}{2}\right)\left.\frac{\partial^2 u}{\partial x^2}\right|_i^n = \alpha\left.\frac{\partial^2 u}{\partial x^2}\right|_i^n \qquad \text{(A1-7)}$$

Thus, we see the artificial viscosity, α is evident in the solution, as if it were explicitly applied as in Eq. (A1-2). For the case when c < 0, the leading error term is:

$$\varepsilon = \left(-c\frac{\Delta x}{2}\right)\left.\frac{\partial^2 u}{\partial x^2}\right|_i^n. \qquad \text{(A1-8)}$$

We confirm that upwinding is a special case of adding artificial viscosity to a central difference scheme by observing the discrete form of the right hand side of Eq. (A1-2):

$$-c\frac{\partial u}{\partial x}+\alpha\frac{\partial^2 u}{\partial x^2}=-c\frac{u_{i+1}^n-u_{i-1}^n}{\Delta x}+\alpha\frac{u_{i+1}^n-2u_i^n+u_{i-1}^n}{\Delta x^2}. \qquad \text{(A1-9)}$$

Substituting $\alpha=c\frac{\Delta x}{2}$ yields:

$$-c\frac{u_{i+1}^n-u_{i-1}^n}{2\Delta x}+\left(c\frac{\Delta x}{2}\right)\frac{u_{i+1}^n-2u_i^n+u_{i-1}^n}{\Delta x^2}=-c\frac{u_i^n-u_{i-1}^n}{\Delta x}, \qquad \text{(A1-10)}$$

which is identical to the upwind difference in Eq. (A1-3) for $c > 0$. Similarly, substituting $\alpha=-c\frac{\Delta x}{2}$ into Eq. (A1-9) yields the upwind difference for $c < 0$.

Appendix 2: Local Sweep Angles

For a tapered wing, the angle of sweep, Λ, varies along the chord. Although one might assume a linear variation in Λ from Λ_{LE} to Λ_{TE}, it is actually $\tan\Lambda$ that varies linearly along the chord, as shown here. This geometric derivation is for a single-element wing. In order to find local values of Λ on a multi-element wing, Λ_{LE} and Λ_{TE} must be known for each element.

Figure A2.1 shows a generic swept, tapered wing. The root chord length is c_r, so for a taper ratio, λ, the tip chord length is $c_t = \lambda c_r$. The wing semispan is b, and a is the distance in the x-direction to the wing tip leading edge due to the leading-edge sweep. From these dimensions, we find relations for the leading-edge and trailing-edge sweep angles:

$$\tan\Lambda_{LE} = \frac{a}{b} \tag{A2-1}$$

$$\tan\Lambda_{TE} = \frac{(a+\lambda c_r) - c_r}{b} = \frac{a + c_r(\lambda - 1)}{b} \tag{A2-2}$$

Solving Eq. (A2-2) for c_r and substituting Eq. (A2-1) for a yields:

$$c_r = \frac{b\tan\Lambda_{TE} - b\tan\Lambda_{LE}}{(\lambda - 1)}. \tag{A2-3}$$

The chordwise location on the airfoil, non-dimensionalized between the leading edge and the trailing edge, is represented by ξ. For an arbitrary chord station, ξ, the local sweep angle, Λ_ξ, is given by:

$$\tan\Lambda_\xi = \frac{(a+\xi\lambda c_r) - \xi c_r}{b} = \frac{a + \xi c_r(\lambda - 1)}{b}. \tag{A2-4}$$

Substituting Eq. (A2-1) for a and Eq. (A2-3) for c_r yields:

$$\tan\Lambda_\xi = \frac{b\tan\Lambda_{LE} + \xi\dfrac{b(\tan\Lambda_{TE} - \tan\Lambda_{LE})}{(\lambda - 1)}(\lambda - 1)}{b}, \tag{A2-5}$$

and simplifying, we find:

$$\tan \Lambda_{\xi} = (1 - \xi) \tan \Lambda_{LE} + \xi \tan \Lambda_{TE}. \qquad \text{(A2-6)}$$

Thus, the tangent of the local sweep varies linearly between the tangent of the leading-edge sweep and the tangent of the trailing-edge sweep.

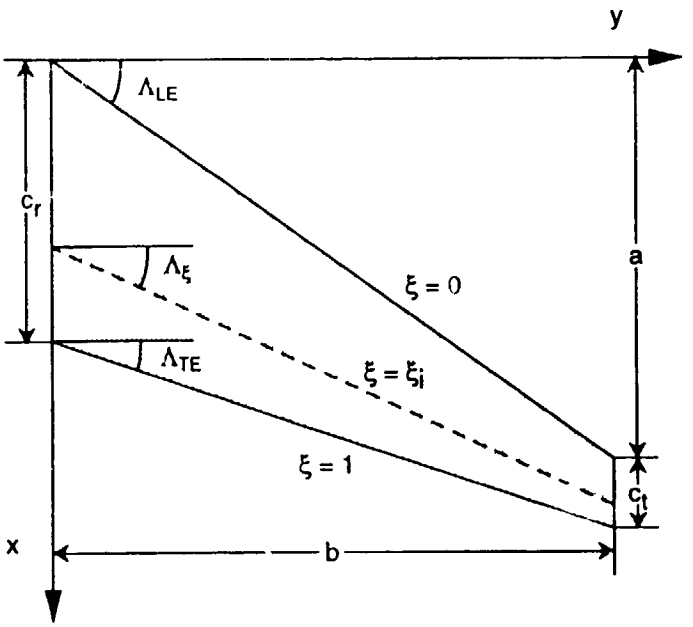

Figure A2.1 - Schematic of a swept, tapered wing.

References:

1 Yip, Long P., Vijgen, Paul M. H. W., Hardin, Jay D., and van Dam, C. P., "In-Flight Pressure Distributions and Skin Friction Measurements on a Subsonic Transport High-Lift Wing Section," in *High Lift System Aerodynamics*, AGARD-CP-515, September 1993, pp. 21/1-19.

2 Thibert, J. J., "The GARTEUR High Lift Research Programme," in *High Lift System Aerodynamics*, AGARD-CP-515, September 1993, pp. 16/1-21.

3 Meredith, P. T., "Viscous Phenomena Affecting High-Lift Systems and Suggestions For Future CFD Development," in *High Lift System Aerodynamics*, AGARD-CP-515, September 1993, pp. 19/1-8.

4 Smith, A. M. O., "Aerodynamics of High-Lift Airfoil Systems," in *Fluid Dynamics of Aircraft Stalling*, AGARD-CP-102, November, 1972, pp. 10/1-27.

5 Smith, A. M. O., "High-Lift Aerodynamics," *Journal of Aircraft*, Vol. 12, No. 6, June 1975, pp. 501-530.

6 Rogers, S. E., "Progress in High-Lift Aerodynamic Calculations," AIAA Paper 93-0194, January 1993.

7 Vatsa, Veer N., et al. "Multi-block Structured Grid Approach for Solving Flows over Complex Aerodynamic Configurations," AIAA Paper 94-0655, January 1994.

8 Mavriplis, D. J., and Martinelli, L., "Multigrid Solution of Compressible Turbulent Flow on Unstructured Meshes Using a Two-Equation Model," AIAA Paper 91-0237, January 1991.

9 Pirzadeh, S., "Unstructured Viscous Grid Generation by Advancing-Layers Method," AIAA Paper 93-3453, August 1993.

10 Mavriplis, Dimitri, "Turbulent Flow Calculations Using Unstructured and Adaptive Meshes," NASA Contractor Report 182102, ICASE Report No. 90-61, September 1990.

11 Bowyer, A., "Computing Dirichlet Tessalations," *The Computer Journal*, Vol. 24, No. 2, 1981, pp. 162-166.

12 Steger, Joseph L., and Chaussee, Denny S., "Generation of Body-Fitted Coordinates Using Hyperbolic Partial Differential Equations," *SIAM J. Sci. Stat. Comput.*, Vol. 1, No. 4, December 1980.

13 Anderson, Dale A., Tannehill, John C., Pletcher, Richard H., Computational Fluid Mechanics and Heat Transfer, Hemisphere Publishing Corporation, New York, 1984.

14 Spalart, P. R., and Allmaras, S. R., "A One-Equation Turbulence Model for Aerodynamic Flows," AIAA Paper 92-0439, January 1992.

15 Valarezo, W. O., and Mavriplis, D. J., "Navier-Stokes Applications to High-Lift Airfoil Analysis," AIAA Paper 93-3534, August 1993.

16 Rogers, S. E., Menter, F. R., Durbin, P. A., and Mansour, Nagi N , "A Comparison Of Turbulence Models In Computing Multi-Element Airfoil Flows," AIAA Paper 94-0291, January 1994.

17 Jameson, A., Schmidt, W., and Turkel, E., "Numerical Solution of the Euler Equations by Finite Volume Methods Using Runge-Kutta Time Stepping Schemes," AIAA Paper 81-1259, 1981.

18 Mavriplis, D. J., and Jameson, A., "Multigrid Solution of the Navier-Stokes Equations on Triangular Meshes," *AIAA Journal*, Vol. 28, No. 8, pp. 1415-1425, August 1990.
19 Venkatakrishnan, V., and Mavriplis, D. J., "Agglomeration Multigrid for the Three-Dimensional Euler Equations," NASA Contractor Report 191595, ICASE Report No. 94-5, January 1994.
20 Anderson, W. Kyle, and Bonhaus, Daryl L., "An Implicit Upwind Algorithm For Computing Turbulent Flows on Unstructured Grids," *Journal of Computers and Fluids*, Vol. 23, No. 1, 1994, pp. 1-21.
21 Chin, V. D., Peters, D. W., Spaid, F. W., and McGhee, R. J., "Flowfield Measurements About a Multi-Element Airfoil at High Reynolds Numbers," AIAA Paper 93-3137, July 1993.
22 Küchemann, F. R. S., The Aerodynamic Design of Aircraft, Pergamon Press, New York, 1976.
23 Hardin, Jay D., Potter, R. C., van Dam, C. P., and Yip, Long P., "Two-Dimensional Computational Analysis of a Transport High-Lift System and Comparison With Flight Test Results," AIAA Paper 93-3533, August 1993.
24 Woodward, D. S., and Lean, D. E., "Where is High-Lift Today? - A Review of Past UK Research Programmes," in *High Lift System Aerodynamics*, AGARD-CP-515, September 1993, pp. 1/1-45.
25 Smith, David G., and Crowder, James P., "The Northern Digital OPTOTRAK for Wind-On Measurement of Model Deflections," Presented at the 71st Semi-Annual Meeting of the Supersonic Tunnel Association, Burbank, California, April 1989.
26 Morgan, Harry L., Jr., "Computer Programs for Smoothing and Scaling Airfoil Coordinates," NASA Technical Memorandum 84666, July 1983.
27 Drela, Mark, "Newton Solution of Coupled Viscous/Inviscid Multielement Airfoil Flows," AIAA Paper 90-1470, Seattle, Washington, June 1990.
28 Narashimha, R., and Sreenivasan, K. R., "Relaminarization of Fluid Flows," *Advances in Applied Mechanics*, Vol. 19, 1979, pp. 201-309.
29 Liebeck, Robert H., "Design of Subsonic Airfoils for High Lift," *Journal of Aircraft*, Vol. 15, No. 9, September 1978, pp. 547-561.
30 Jang, Cory S., Ross, James C., and Cummings, Russell M., "Computational Evaluation of an Airfoil with a Gurney Flap," AIAA Paper 92-2708, June 1992.